Journal of CO_2 Utilization 21 (2017) 368–382

Contents lists available at ScienceDirect

Journal of CO_2 Utilization

journal homepage: www.elsevier.com/locate/jcou

Thermal management of a Sabatier reactor for CO_2 conversion into CH_4: Simulation-based analysis

Duo Sun, David S.A. Simakov*

Department of Chemical Engineering, University of Waterloo, Waterloo, ON, N2L 3G1, Canada

ARTICLE INFO

Keywords:
CO_2
Renewable natural gas
Sabatier reactor
Molten salt

ABSTRACT

Converting CO_2-rich waste streams such as raw biogas, landfill gas and power plant flue gas into synthetic fuels and chemicals will reduce greenhouse gas emissions, providing revenue at the same time. One option is to convert CO_2 into CH_4 by hydrogenation via Sabatier reaction. This synthetic methane will be renewable if the H_2 required for the reaction is generated via water electrolysis using solar and wind energy or hydroelectricity. However, to realize the potential of this approach, a number of technological challenges related to the Sabatier reactor design have to be resolved, including thermal management. The high exothermicity of the Sabatier reaction can lead to reactor overheating. High temperatures are unfavorable to the exothermic and reversible methanation process, resulting in low CO_2 conversions. A simulation-based study of a Sabatier reactor was performed in order to optimize the removal of heat, while maximizing CO_2 conversion and CH_4 production. The heat-exchanger type packed bed reactor with internal cooling by a molten salt was simulated using a transient, pseudo-homogeneous mathematical model. Reactor performance was evaluated in terms of CO_2 conversion and CH_4 yield. The simulation results show that feed temperature, feed flow rate, and molten salt flow rate are the crucial parameters affecting the reactor performance. For the optimized operating conditions, the model predicts CO_2 conversions and CH_4 yields above 90% at high reactor throughputs, with space velocities up to 10,000 h^{-1}. A preliminary techno-economic evaluation is provided: opportunities and challenges are outlined.

1. Introduction

The intensive use of fossil fuels leads to growing CO_2 emissions that accelerate Global Warming. It is absolutely necessary to capture anthropogenic CO_2. Once captured, CO_2 can be stored (e.g., in geological formations) but this approach requires high capital and operating costs, hindering its widespread commercialization. The alternative to CO_2 storage is CO_2 conversion into synthetic fuels and chemicals that closes the artificial carbon cycle. Being a harmful greenhouse gas, CO_2 is also an excellent source of carbon, non-flammable and non-corrosive. Resources are abundant, including flue gases from coal- and natural gas-fired power plants, biogas and landfill gas (up to 40% CO_2), and off-gas streams in several industrial processes such as ammonia production and fermentation. There are also large resources of CO_2 accompanying natural gas and oil production wells; this CO_2 is typically vented into the atmosphere.

Conversion of captured CO_2 into synthetic fuels and chemicals is an attractive avenue for reduction of CO_2 emissions and, as such, this topic has attracted the interest of many research groups around the world [1–3]. Many research efforts have focused on photochemical and electrochemical reduction of CO_2 into a variety of products, including formic acid and methanol, in an aqueous environment using water as a source of H_2 for CO_2 reduction [1,2]. This approach is apparently attractive as it only uses water and CO_2 as the starting materials and the sun and (potentially) renewable electricity as a source of energy. However, photochemical CO_2 reduction has inherent limitations of solar energy utilization, while electro-chemical reduction of CO_2 has low efficiencies of electricity utilization. Both processes are limited by low CO_2 solubility in water and have severe diffusion limitations [1,2].

An alternative approach is thermocatalytic conversion that combines the use of high temperatures with a heterogeneous catalyst, providing fast reaction rates and, therefore, allowing for large volume production [3]. One of the thermocatalytic routes for CO_2 conversion is methanation, also called the Sabatier reaction [3,4]. This reaction converts CO_2 into CH_4 by hydrogenation, Eqs. (1)-(3) below. This synthetic methane will be renewable if the H_2 required for the reaction is produced via water electrolysis using renewable electricity (solar, wind, or hydro), making the process sustainable. Despite the abundance of natural gas in certain countries (also thanks to fracking) and current low prices of fossil methane, CO_2 conversion into renewable natural gas

* Corresponding author.
E-mail address: dsimakov@uwaterloo.ca (D.S.A. Simakov).

http://dx.doi.org/10.1016/j.jcou.2017.07.015
Received 14 October 2016; Received in revised form 23 June 2017; Accepted 17 July 2017
Available online 18 August 2017

Nomenclature

$a_{c,HE}$	Cooling tube surface-to-volume ratio, m^{-1}
$a_{r,HE}$	Cooling tube surface-to-packed volume ratio, m^{-1}
$a_{r,HL}$	Reactor surface-to-volume ratio, m^{-1}
A_c	Total cross-sectional area of cooling tubes, m^2
A_j	Pre-exponential factor of the rate coefficient of reaction j, units of k_j
B_j	Pre-exponential factor of the adsorption coefficient of species i, units of K_j
C_i	Molar concentration of species i, mol/m^3
C_t	Total molar concentration, mol/m^3
C_{pc}	Coolant heat capacity, kJ/(kg K)
C_{pg}	Gas heat capacity, kJ/(mol K)
d	Wall thickness, m
d_p	Catalytic pellet diameter, m
D	Diameter, m
D_{ae}	Effective axial dispersion coefficient, m^2/s
D_m	Gas molecular diffusivity, m^2/s
E_j	Activation energy of reaction j, kJ/mol
F_i	Molar flow rate of species i, mol/s
F_{tf}	Total feed molar flow rate, mol/s
G	Gravimetric (mass) flow rate, kg/s
h_{nc}	Natural convection heat transfer coefficient, $kJ/(m^2\ s\ K)$
h_w	Effective wall heat transfer coefficient, $kJ/(m^2\ s\ K)$
ΔH_i	Adsorption enthalpy change of species i, kJ/mol
k_{ae}	Effective axial heat dispersion coefficient, kJ/(m s K)
k_j	Rate constant of reaction j
K_i	Adsorption constant of species i, bar^{-1}
$K_{j,eq}$	Equilibrium constant of reaction j
L	Reformer length, m
N_c	Number of cooling tubes
Nu	Nusselt number
p_i	Partial pressure of gaseous species i, bar
P	Pressure, bar
Pr	Prandtl number
Re	Reynolds number
R_j	Rate of reaction j, mol/(kg s)
R_g	Gas constant, kJ/(mol K)
$GHSV$	Gas hourly space velocity, h^{-1}
t	Time, s
T	Reactor temperature, K
T_c	Coolant temperature, K
T_e	Environment temperature, K
U_w	Overall effective wall heat transfer coefficient, $kJ/(m^2\ s\ K)$
v	Fluid velocity, m/s
V	Compartment volume, m^3
y_i	Mole fraction of species i
z	Reactor length coordinate, m

Greek letters

ε	Packed bed porosity
ϕ	Thiele modulus
η_j	Effectiveness factor of reaction j
η_{ST}	Steam turbine efficiency
λ	Thermal conductivity, kW/(m K)
μ	Viscosity, kg/(m s)
ρ_c	Coolant density, kg/m^3
ρ_g	Gas molar density, mol/m^3
ρ_s	Solid density, kg/m^3
τ_b	Packed bed tortuosity

Subscripts

c	Coolant
eff	Effective
eq	Equilibrium
f	Feed
g	Gas
HE	Heat exchange
HL	Heat loss
int	Initial
MS	Molten salt
nc	Natural convection
PB	Packed bed
s	Solid
r	Reactor

(RNG) is still a useful strategy.

First, this approach creates an artificial carbon cycle (similar to photosynthesis if solar energy is used for H_2 production) recycling the otherwise emitted CO_2 in our energy distribution systems and, therefore, reducing the consumption of the fossil methane (natural gas). Second, the produced RNG can be injected into the existing natural gas infrastructure that provides virtually unlimited storage and transportation capacities not only for renewable energy but also for surplus and off-peak electricity. Third, converting CO_2 into RNG can provide local energy independence, while RNG can be used as a transportation fuel as well. Eventually, the renewable methane is combusted to produce power and heat, and CO_2. This CO_2 can be potentially captured and converted back into RNG using renewable energy, thus using this carbon as a renewable energy carrier. Even though re-capturing of CO_2 might be unsuitable in the near future for some uses, such as residential heating, recycling the carbon captured from waste streams (in form of CO_2) one more time as an energy carrier can reduce the consumption of fossil methane significantly. The price of the produced RNG is of course a concern; this issue is addressed in Section 3.4.

The strongly exothermic Sabatier reaction, Eq. (1), is typically accompanied by the mildly endothermic reverse water gas shift, Eq. (2), and the exothermic CO methanation, Eq. (3).

$$CO_2 + 4H_2 \rightleftarrows CH_4 + 2H_2O \quad \Delta H^\circ_{298} = -164.9\ \text{kJ/mol} \tag{1}$$

$$CO_2 + H_2 \rightleftarrows CO + H_2O \quad \Delta H^\circ_{298} = 41.2\ \text{kJ/mol} \tag{2}$$

$$CO + 3H_2 \rightleftarrows CH_4 + H_2O \quad \Delta H^\circ_{298} = -206.1\ \text{kJ/mol} \tag{3}$$

The overall process is highly exothermic which requires efficient heat removal, in order to facilitate CH_4 production. In addition to this thermodynamic constrain, reactor overheating can also lead to fast catalyst deactivation by sintering and coking. For nickel-based catalysts, operating temperatures should be kept below 550 °C to prevent catalyst deactivation [5]. Historically, methanation systems were designed for conversion of synthesis gas [6], but, recently, CO_2 was also considered as a feedstock for methanation [5]. Two conventional configurations of methanation reactors are fixed bed [7–11] and fluidized bed [12–14]. Microchannel reactors [15], monolith reactors [16–18], and three-phase slurry reactors [19,20] were also suggested as design solutions for carrying out methanation reactions. A comprehensive overview of the abovementioned concepts is available in the literature [21]. One of the most challenging problems in the design of methanation reactors is thermal management.

For the adiabatic fixed bed reactor design, the primary approach is to use cascades of adiabatic reactors (typically 2–6) with intermediate cooling and gas recirculation [21]. Though such systems can efficiently control the process temperature, the use of multiple reactors, recycle compressors, heat exchangers etc. results in system complexity and high capital cost investment. An alternative approach is to use a cooled

packed-bed reactor [9,10]. This method could potentially allow performing methanation as a single-stage process but heat removal optimization to avoid the hot spot formation is a difficult task. Structured, microchannel and monolith reactors [15–18] have been developed to overcome the problems of temperature control and overheating in conventional packed-bed reactors. However, while improved heat transfer characteristics and, ideally, nearly-isothermal operation significantly simplify process control, the reactor itself becomes more expensive because of the complicated deposition of the catalyst coating and the difficulty of replacing deactivated catalyst.

Fluidized-bed reactors [12–14] are widely suggested as ideal isothermal reactors due to the excellent transport characteristics, allowing for the use of a single reactor and simplifying process control. However, catalyst attrition remains a major obstacle toward implementation of fluidized beds. Another disadvantage is that fluidized-bed reactors can only be operated in a narrow range of operating conditions dictated by the fluidization velocity, restricting reactor throughputs. Three-phase methanation reactors [19,20] provide excellent heat transfer characteristics, allowing isothermal operation, but are restricted to a narrow operating window dictated by solvent/heat transfer fluid properties. Other major drawbacks are the gas-to-liquid mass transfer resistance and the fluid decomposition and evaporation.

The actively-cooled packed bed reactor design can potentially provide a low-cost solution for the single-pass methanation process. However, heat removal optimization is required. Recently reported modeling studies did not account for coolant temperature variations, assuming constant temperature of the heat transfer fluid [9,10]. Such situation is only achievable when the heat transfer fluid flow rate is very high [22]. On the other hand, process optimization will require minimizing the coolant flow rate, maximizing at the same time the reactor performance.

In the presented herein study, the heat-exchanger type Sabatier reactor cooled by molten salt is investigated via numerical simulations in order to optimize the removal of heat, while maximizing CO_2 conversion and CH_4 production rate. Molten salts are advantageous over conventional heat carriers, such as steam and mineral oils, due to higher operating temperatures, low working pressure, non-flammability, high density and heat capacity, and, importantly, good heat conductivity [22]. Mineral oils are unsuitable for removing heat from the Sabatier reactor due to high operating temperature. Temperatures above 700 K are required to achieve high CO_2 conversions in the Sabatier reaction (as it is shown by numerical simulations below). However, maximum temperatures for mineral oil-based heat transfer fluids do not exceed 600 K. At higher temperatures, these heat transfer fluids will decompose. Steam can be theoretically used at high temperatures. However, it will require extremely high pressures to use saturated steam which has good heat transfer characteristics. Regardless, handling large amounts of steam, which can cause corrosion, fouling and scaling, is rather disadvantageous from the operating point of view.

Molten salts, on the other hand, have their own disadvantages. Molten salt can solidify if the temperature is below the melting point, clogging the tubes. Also, there is an upper limit of operation above which thermal decomposition will occur. To sum up, molten salts could be highly-efficient heat transfer fluids for heat removal from a Sabatier reactor, due to their high heat capacity, excellent heat transfer characteristics and suitable operating temperature range. For similar reasons, molten salts were suggested as a highly-efficient heat transfer fluid for the low-temperature solar reforming which has similar operating temperature range [22–24].

A conceptual representation of the entire methanation system comprising the molten-salt cooled Sabatier reactor is shown in Fig. 1. Hydrogen which is required for the Sabatier reaction can be generated using renewable energy [25,26]. The reaction heat removed from the reactor by the heat transfer fluid can be used to preheat the feed, and can be also utilized for electricity generation and residential heating, Fig. 1. In our study we focus first on the mathematical analysis of the Sabatier reactor via numerical simulations. The reactor performance is evaluated in terms of CO_2 conversion and CH_4 yield as a function of operating parameters, such as feed temperature, feed flow rate, and molten salt flow rate. We performance a sensitivity analysis and a

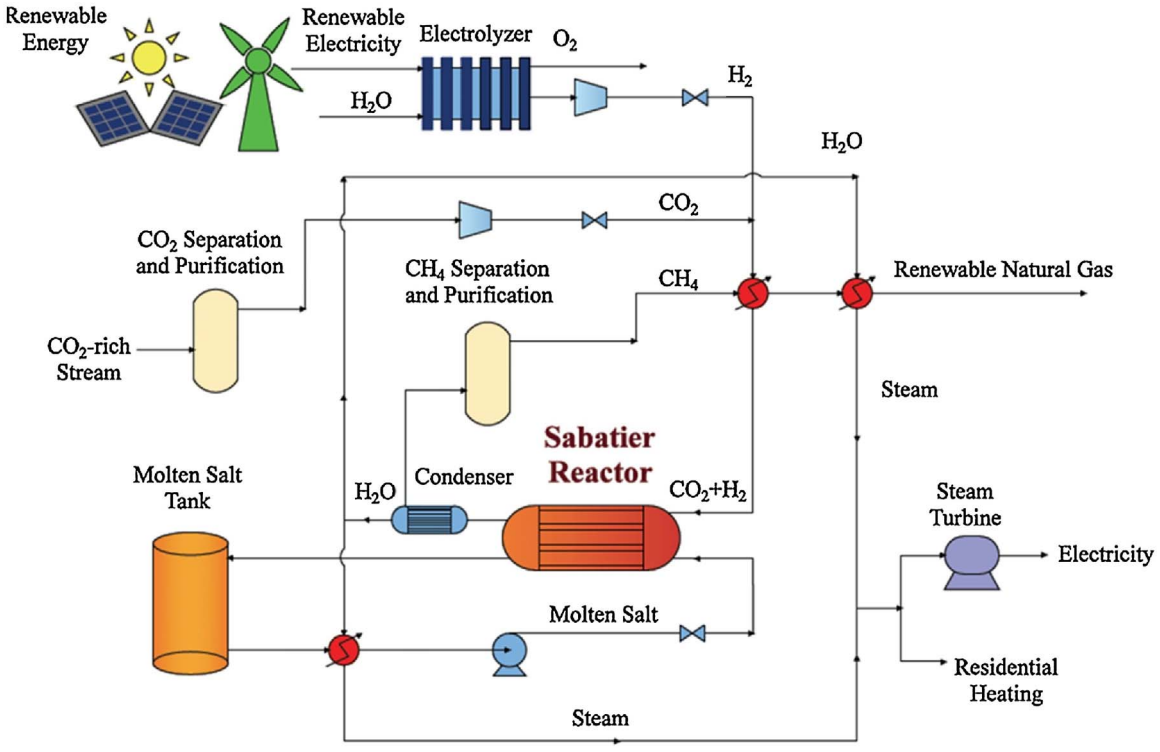

Fig. 1. Conceptual process flow diagram of the renewable natural gas generation system. The Sabatier reactor converts a mixture of CO_2 and H_2 into CH_4 and water. The reaction heat is removed from the reactor by the molten salt recirculation system.

preliminary optimization aimed at maximizing the reactor throughput and CH_4 yield. Finally, based on the output from the reactor analysis, we perform a preliminary techno-economic evaluation at the system level. The purpose of this assessment is to estimate the economic viability of the renewable natural gas (RNG) production using the analyzed reactor as an essential component of the integrated system.

2. Model formulation

The suggested Sabatier reactor design is shown in Fig. 2. The reactor is a heat-exchanger type packed bed internally cooled by molten salt flowing in multiple cooling tubes. To minimize uncontrollable heat losses to the environment, the reactor is insulated by a layer of quartz wool. Both the external and internal tubes are made of stainless steel. The dimensions used in numerical simulations are listed in Table 1.

Since we used a one-dimensional mathematical model in our study, we selected reactor dimensions in such a way that the radial reactor dimension is as small as possible. In order to minimize the heat transfer distance (to reduce the space between the cooling tubes), the minimum number of cooling tubes was set to $N_c = 12$. For this number of tubes and for the dimensions described in Table 1 with evenly distributed tubes, the distance between any two adjusted cooling tubes will be 19 ± 1 mm for $N_c = 12$. Thermal conductivity of the packed bed should prevent large radial gradients over that relatively small distance [11]. The maximum of $N_c = 22$ was set to allow enough space for catalytic pellets between the cooling tubes. Due to the high thermal conductivity of the molten salt, significant radial gradients are not expected to develop within the coolant tubes ($D_c = 0.02$ m) [22].

Due to the high volumetric heat capacity of the molten salt, only a relatively small fraction of the total reactor volume is required for the molten salt compartment (Table 1). The total reactor volume for the suggested dimensions is approximately 30 L, which is suitable for medium scale applications. As it is later discussed in Section 3.4, the single reactor is predicted to provide up to 100–500 kW power output, providing a potential for MW-scale applications using multiple reactors. A modular, multiple reactor parallel operation will be advantageous for maintenance, since reactors can be conditioned or replaced without shutting down the entire process.

A transient, one-dimensional, pseudo-homogeneous mathematical model [27,28] was used to simulate the reactor. As opposed to assuming constant coolant temperature [9,10], the model accounts for temperature variations in the heat transfer fluid. The model also includes the axial mass and heat dispersion, and accounts for the temperature dependence of thermo-physical properties. Component mass balance and energy balance for the packed bed compartment are given by Eqs. (4) and (5), respectively; the temperature distribution in a single molten salt tube is described by Eq. (6). The corresponding boundary and initial conditions are listed in Eqs. (7) and (8). Ideal gas behavior was assumed to calculate an average gas density. For the conditions used in our simulations the difference between the average molar density calculated from tabulated gas densities and the one calculated from the ideal gas law was negligible. Pressure drop was calculated using Ergun equation, Eq. (9), with a fixed inlet pressure (adjusted by a back pressure regulator in a practical situation). Variations in the gas velocity due to change in number of moles are considered by Eq. (10) [29]. Effective heat capacity in Eq. (5) is defined by Eq. (11); N_c is the number of cooling tubes.

$$\varepsilon\frac{\partial C_i}{\partial t} = D_{ae}\frac{\partial^2 C_i}{\partial z^2} - \varepsilon v_g\frac{\partial C_i}{\partial z} + \rho_s(1-\varepsilon)\sum_j \eta_j R_{ij} \tag{4}$$

$$(\rho C_p)_{eff}\frac{\partial T}{\partial t} = k_{ae}\frac{\partial^2 T}{\partial z^2} - \varepsilon\rho_g C_{pg} v_g\frac{\partial T}{\partial z} + \\ + \rho_s(1-\varepsilon)\sum_j (-\Delta H_j)\eta_j R_j - N_c U_{w,HE} a_{r,HE}(T - T_c) \\ - U_{w,HL} a_{r,HL}(T - T_e) \tag{5}$$

$$\rho_c C_{pc}\frac{\partial T_c}{\partial t} = \lambda_c\frac{\partial^2 T_c}{\partial z^2} - \rho_c C_{pc} v_c\frac{\partial T_c}{\partial z} - U_{w,HE} a_{c,HE}(T_c - T) \tag{6}$$

$$\begin{aligned} &z = 0 \quad \varepsilon v_{gf}(C_{i,f} - C_i) = -D_{ae}\frac{\partial C_i}{\partial z} \qquad z = L \quad \frac{\partial C_i}{\partial z} = 0 \\ &\varepsilon\rho_g v_{gf} C_{pg}(T_f - T) = -k_{ae}\frac{\partial T}{\partial z} \qquad \frac{\partial T}{\partial z} = 0 \\ &\rho_c v_{cf} C_c(T_{c,f} - T_c) = -k_c\frac{\partial T_c}{\partial z} \qquad \frac{\partial T_c}{\partial z} = 0 \end{aligned} \tag{7}$$

$$\begin{aligned} &at\ t = 0: \quad C_i(0, z) = C_{i,\text{int}} \\ &T(0, z) = T_{\text{int}} \\ &T_c(0, z) = T_{c,\text{int}} \end{aligned} \tag{8}$$

$$\frac{dP}{dz} = -150\frac{(1-\varepsilon)^2\mu_g}{d_p^2\varepsilon^3}v_g - 1.75\frac{(1-\varepsilon)\rho_g}{d_p\varepsilon^3}v_g^2 \quad P(0) = P_{lf} \tag{9}$$

$$v_g(z) = v_{gf}\frac{\sum_i C_i(z)}{\sum_i C_{i,f}} \tag{10}$$

$$(\rho C_p)_{eff} = \varepsilon\rho_g C_{pg} + (1-\varepsilon)\rho_s C_{ps} \tag{11}$$

2.1. Kinetics

Reaction rates are calculated using the commonly adopted kinetics

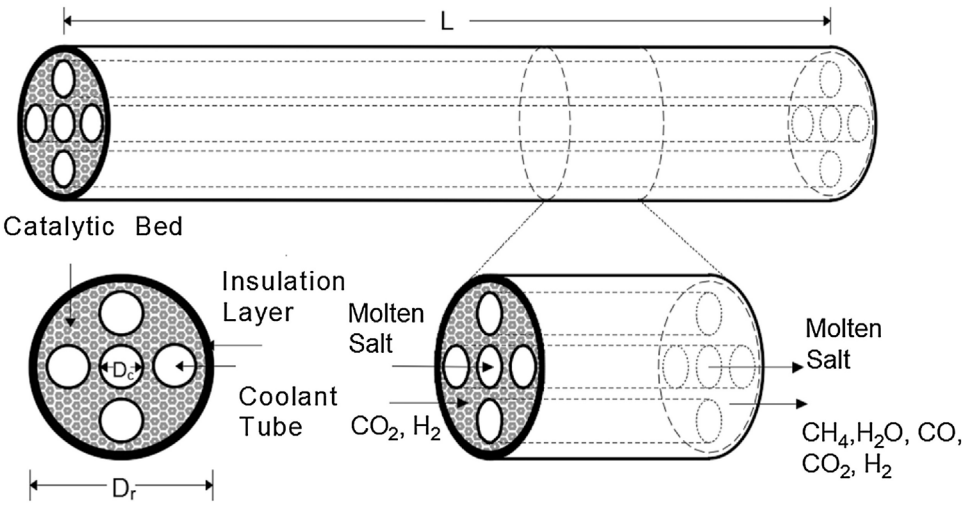

Fig. 2. Schematic of the molten salt-cooled, heat-exchanger type packed bed Sabatier reactor.

Table 1
Reactor dimensions.

D_r (m)	D_c (m)	d_w (m)	d_{iw} (m)	d_p (m)	N_c	L (m)	V_{PB} (m^3)	V_{MS} (m^3)
0.2	0.02	0.002	0.05	0.003	12–22	1	0.0255	0.0041

D_r and D_c denote the diameter of the packed bed (D_r) and coolant (D_c) compartments. L is the reactor length and N_c is the number of the molten salt coolant tubes. d_w denotes the thickness of the reactor wall and cooling tube, correspondingly; d_{iw} is the insulation layer thickness. V denotes the volume of the packed bed (V_{PB}) and coolant (molten salt) (V_{MS}) compartments; d_p is the catalytic pellet diameter.

for methane steam reforming over the Ni/Al_2O_3 catalyst [30,31], Eqs. (12a)–(12c). The kinetic expressions account for the reversibility of the reforming and water gas shift reactions and can be used therefore for modeling the CO_2 methanation reaction system, Eqs. (1)–(3). All parameters are tabulated in the literature, e.g., see Tables 3 and 4 in Rodríguez et al. [32]. Intraparticle and interphase transport limitations can be neglected for the size of catalytic pellets used in our simulations (d_p = 3 mm, Table 1) [28].

$$R_1 = \frac{k_1}{p_{H_2}^{2.5}}\left(p_{CH_4}p_{H_2O} - \frac{p_{H_2}^3 p_{CO}}{K_{1,eq}}\right)\frac{1}{\text{den}^2} \tag{12a}$$

$$R_2 = \frac{k_2}{p_{H_2}}\left(p_{CO}p_{H_2O} - \frac{p_{H_2}p_{CO_2}}{K_{2,eq}}\right)\frac{1}{\text{den}^2} \tag{12b}$$

$$R_3 = \frac{k_3}{p_{H_2}^{3.5}}\left(p_{CH_4}p_{H_2O}^2 - \frac{p_{H_2}p_{CO_2}}{K_{3,eq}}\right)\frac{1}{\text{den}^2} \tag{12c}$$

$$\text{den} = 1 + K_{CO}p_{CO} + K_{H_2}p_{H_2} + K_{CH_4}p_{CH_4} + \frac{K_{H_2O}p_{H_2O}}{p_{H_2}}$$

$$k_j = A_j \exp\left(\frac{-E_j}{R_g T}\right)$$

$$K_i = B_i \exp\left(\frac{-\Delta H_i}{R_g T}\right)$$

The internal effectiveness factor was calculated using the standard expression for a spherical pellet [33], with the Thiele modulus defined for each reaction with the corresponding reaction rate constant (k_j in Eq. (12)):

$$\eta_j = \frac{3}{\phi_j}\left(\frac{1}{\tanh\phi_j} - \frac{1}{\phi_j}\right); \qquad \phi_j = \sqrt{\frac{\hat{k}_j d_p^2}{4D_m}}$$

$$\hat{k}_1 = \frac{k_1\rho_s(1-\varepsilon)}{\sqrt{P_{tf}}\rho_g\varepsilon}; \qquad \hat{k}_2 = \frac{k_2\rho_s(1-\varepsilon)P_{tf}}{\rho_g\varepsilon}; \qquad \hat{k}_3 = \frac{k_3\rho_s(1-\varepsilon)}{\sqrt{P_{tf}}\rho_g\varepsilon} \tag{13}$$

2.2. Transport parameters

The effective axial mass dispersion coefficient is calculated using the following correlation [34]:

$$D_{ae} = \varepsilon\left(\frac{D_m}{\tau_b} + 0.5 d_p v_g\right); \quad \tau_b = \frac{1}{\varepsilon^{0.5}} \tag{14}$$

The expression for the effective axial heat dispersion coefficient (k_{ae}), Eq. (15), was derived from the heat conductivity correlations developed for catalytic fixed beds [27,35,36]. Values of k_{ae} were calculated using original correlations [35,36] in the relevant range of parameters, plotted versus particle Reynolds number (Re_p), and fitted using least squares analysis, resulting in the following correlation:

$$k_{ae} = \lambda_g(8 + 0.05\,\text{Re}_p^{1.09}); \quad \text{Re}_p = \frac{v_g\rho_g d_p}{\mu_g} \tag{15}$$

Wall heat transfer coefficients are determined by resistances in series:

$$U_{w,HE} = \left(\frac{1}{h_{wr}} + \frac{d_w}{\lambda_w} + \frac{1}{h_{wc}}\right)^{-1} \tag{16a}$$

$$U_{w,HL} = \left(\frac{1}{h_{wr}} + \frac{d_w}{k_w} + \frac{d_{iw}}{k_{iw}} + \frac{1}{h_{nc}}\right)^{-1} \tag{16b}$$

The wall heat exchange coefficient between the catalytic bed and the coolant tube, $U_{w,HE}$, accounts for resistances of the fixed bed, the coolant tube wall, and the molten salt, Eq. (16a). Similarly, the correlation for the wall heat transfer coefficient, $U_{w,HL}$, accounts for resistances through the catalytic bed, the reactor wall, the quartz wool insulation layer (Fig. 1) [37], accounting also for natural convection (h_{nc}) [38]. Since the insulation layer natural convection resistances are dominant in Eq. (16b), the wall heat transfer coefficient was nearly constant in all simulations: $U_{w,HL} \approx 0.01$ W/(m^2 K).

The effective wall heat transfer coefficient for the reaction compartment (h_{wr}) is estimated using the following correlation obtained in the similar way as Eq. (15), using a complete set of the original correlations [27,28,35,36]:

$$Nu_p = \frac{h_{wr}d_p}{\lambda_g} = 24 + 0.34\,\text{Re}_p^{0.77}; \quad \text{Re}_p = \frac{v_g\rho_g d_p}{\mu_g} \tag{17}$$

The effective wall heat transfer coefficient for the coolant tube (h_{wc}) is estimated using the following correlations [39–41]:

$$\textit{for } \text{Re}_c < 2030: \quad Nu_c = 3.66 + \frac{0.065\,\text{Re}_c\text{Pr}_c(D_c/L)}{1 + 0.04[\text{Re}_c\text{Pr}_c(D_c/L)]^{2/3}} \tag{18a}$$

$$\textit{for } 2030 < \text{Re}_c < 4000: \quad Nu_{wc} = 0.012(\text{Re}_c^{0.87} - 280)\text{Pr}_c^{0.4}[1 + (D_c/L)^{2/3}] \tag{18b}$$

$$\textit{for } \text{Re}_c > 4000: \quad Nu_c = 0.027\,\text{Re}_c^{0.8}\,\text{Pr}_c^{1/3} \tag{18c}$$

$$Nu_{wc} = \frac{h_{wc}D_c}{\lambda_c}; \quad \text{Re}_c = \frac{v_c\rho_c D_c}{\mu_c}; \quad \text{Pr}_c = \frac{C_{pc}\mu_c}{\lambda_c}$$

2.3. Numerical procedure

The model was solved using the MATLAB PDE solver with a second-order accurate spatial discretization based on a fixed set of user-specified nodes and time integration done by the stiff ODE solver (ode 15s). Dependences of thermophysical properties (density, viscosity, heat capacity, diffusivity, and thermal conductivity) on temperature, pressure and composition were accounted for using polynomial regressions fitted to the data on thermophysical properties from the literature [39,42–44]. Molten salt properties were adopted from the data on commercially available molten salts (Dynalene, Inc. [45], Dynalene MS-2).

3. Results and discussion

Reactor performance was evaluated via numerical simulations as a function of operating parameters, in terms of CO_2 conversion (X_{CO2}), selectivity to CH_4 (S_{CH4}), and CH_4 yield (Y_{CH4}):

$$X_{CO_2} = \frac{y_{CH_4} + y_{CO}}{y_{CH_4} + y_{CO} + y_{CO_2}} \tag{19}$$

$$S_{CH_4} = \frac{y_{CH_4}}{y_{CH_4} + y_{CO}} \tag{20}$$

$$Y_{CH_4} = \frac{y_{CH_4}}{y_{CH_4} + y_{CO} + y_{CO_2}} \quad (21)$$

Outlet conversion, selectivity and yield are calculated based on the outlet mole fractions. In all simulations, the feed pressure was 500 kPa and the feed composition was set to the molar stoichiometric ratio of $H_2/CO_2 = 4$. The molten salt feed temperature was set to its minimum operating temperature of 415 K [45]. All parameters are listed in Table 2.

Variable operating parameters included initial temperature (T_{int}), gas stream feed temperature (T_f), gas hourly space velocity (GHSV), and the normalized cooling rate ($G_c/G_{c,0}$). Gas hourly space velocity (volumetric feed flow rate divided by the packed bed volume) is defined as follows:

$$GHSV = \frac{\varepsilon v_{gf}}{L} \quad (22)$$

The reference molten salt gravimetric flow rate is calculated assuming that the heat generation rate (for complete CO_2 conversion and no CO formation) is equal to the rate of heat removal by the molten salt (assuming that $\Delta T_{MS} = 300$ K; the operating range of the molten salt is 415–758 K [45]):

$$G_{MS,0} = \frac{y_{CO_2}\Delta H_{SR} F_{tf}}{C_{pc}\Delta T_{MS}}; \quad F_{tf} = \rho_{gf} V_{PB} GHSV \quad (23)$$

3.1. Model validation: approach to equilibrium

For long residence times, i.e. low space velocity, it is expected that the reactor performance would approach equilibrium. Comparison between the simulation results obtained at GHSV = 100 h^{-1} and equilibrium data [46] is shown in Fig. 3, in terms of CO_2 conversion and selectivity to CH_4 formation (parameters are listed in the figure caption). Good agreement with the equilibrium data was obtained. CO_2 conversion is favored by high pressures and low temperatures; CH_4 selectivity drops rapidly for $T > 850$ K.

Because of a combined effect of the decrease of conversion and selectivity with increasing temperatures, CH_4 yield drops rapidly for $T > 800$ K, Fig. 4. Therefore, thermal management of the Sabatier process is crucial. Reactor temperature should be kept sufficiently high to accelerate catalytic reactions, but below 900 K, when considerably high CH_4 yield is achievable at slightly elevated pressures, Fig. 4. Moreover, for the reactor configuration studied here, molten salt operating range becomes a crucial parameter. The coolant feed temperature should be obviously kept above the molten salt melting point but also well below the temperature of its thermal decomposition. The recommended operating range for the type of molten salt used in the simulations is 415–758 K, which is a typical operating range for molten salts (some molten salts can be operated at slightly higher temperature but have higher freezing point, e.g., 500–838 K) [45]. The upper range of this temperature regime is also favorable for CH_4 formation, Fig. 4.

3.2. Spatial profiles within the reactor

Typical spatial reactor profiles are presented in Fig. 5, showing the reactor ignition (Fig. 5a) and stationary spatial profiles of temperatures and mole fractions. For the set of parameters listed in Fig. 5, ignition occurs approximately at the first third of the reactor length, with subsequent formation of a stationary thermal front after approximately 5 min of simulated time, Fig. 5a. The simulation predicts that steady state temperatures are identical in the packed bed and molten salt compartments, except for the small area at the temperature front, Fig. 5b.

Importantly, the molten salt temperature varies significantly as a function of the reactor length. This observation emphasizes the importance of accounting for the coolant temperature as a variable, not a constant parameter. Variations of the coolant temperature within the reactor will lead to variations of the heat transfer flux, affecting therefore the thermal distribution within the reactor. As heat is being transferred from the packed bed to the coolant, the molten salt temperature increases decreasing the inter-compartment temperature difference which is the driving force for the heat transfer. Mole fraction profiles form a sharp front coinciding with temperature distribution, Fig. 5c, d. CO_2 and H_2 are mainly consumed at the front, producing mainly CH_4 and H_2O, as well as a small fraction of CO. Downstream the reactor, there is additional consumption of H_2, as CO is converted via methanation, Eq. (3). Since the methanation reaction is highly exothermic, downstream cooling will be crucial for reactor performance, as discussed in Section 3.3.4.

Increasing the inlet temperature of the feed gas mixture (T_f) shifts the location of the thermal front towards the reactor entrance, Fig. 6b. Reactor performance change accordingly (lower panels in Fig. 6). Slightly higher CH_4 yield is obtained for higher feed temperature, but in overall very similar performance is predicted in both cases, Fig. 6. However, the case shown in Fig. 6a is expected to be less beneficial for reactor operation. First, almost a third of the reactor stays cold with no reactions occurring there. Second, a thermal front located at some location within the reactor may be unstable and prone to downstream propagation which can result in reactor extinction, as discussed in Section 3.3.2.

3.3. Reactor performance

Reactor performance was evaluated as a function of variable parameters listed in Table 2: initial (start-up) temperature (T_{int}), inlet temperature of the feed mixture (the composition is $H_2/CO_2 = 4$, Table 2) (T_f), gas hourly space velocity (GHSV), and the molten salt gravimetric flow rate (G_{MS}) normalized to the reference rate ($G_{MS}/G_{MS,0}$). Initial and feed temperatures are expected to affect the reactor performance significantly because of the high exothermicity of the Sabatier reaction system, Eqs. (1)–(3). Feed flow rates in the reaction and coolant compartments (GHSV and G_{MS}) will be crucial parameters, defining the rates of heat generation and removal.

3.3.1. Start-up temperature

Though the Sabatier reaction is highly exothermic, preheating will be required in a practical situation in order to ignite the reactor (an example of the simulated reactor ignition is shown in Fig. 5a). The effect of the initial (start-up) temperature is shown in Fig. 7: outlet temperatures, conversion, selectivity, and yield are plotted versus initial temperature. It is assumed that the entire reactor is heated to the same temperature, which can be achievable by flowing the molten salt through the cooling tubes before feeding the gas mixture. There is a sharp threshold temperature of 545 K. Above this temperature, reaction ignition takes place, while further increase in the preheating temperature has virtually no effect on the reactor performance.

3.3.2. Effect of feed temperature

The gas feed temperature (T_f) is a crucial operating parameter affecting the temperature distribution within the reactor, Fig. 6. It is expected that below a certain threshold feed temperature reactions will

Table 2
Operating conditions.

P_f (kPa)	H_2/CO_2	T_{cf} (K)	T_{int} (K)	T_f (K)	GHSV (h^{-1})	$G_{MS}/G_{MS,0}$
500	4/1	415	500–600	450–650	100–50,000	0.1–1

P_f denotes the feed pressure and H_2/CO_2 is the molar feed ratio of H_2 to CO_2. T_{cf} stands for the coolant (molten salt) feed temperature. T_{int} and T_f are initial (start-up) and gas feed temperatures, respectively. GHSV is the gas hourly space velocity, Eq. (22). $G_{MS}/G_{MS,0}$ stands for the normalized gravimetric flow rate of the molten salt, Eq. (23).

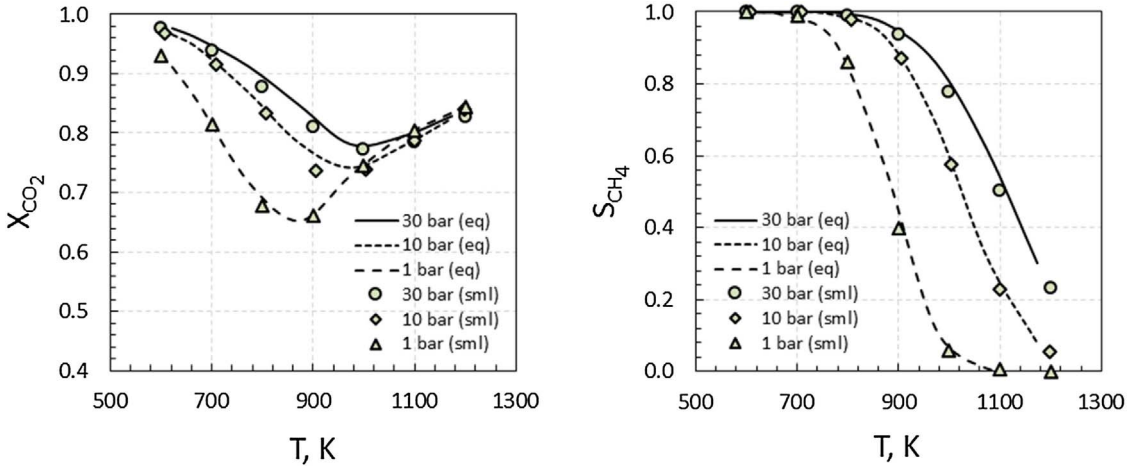

Fig. 3. Approach to equilibrium: CO_2 conversion (X_{CO2}) and selectivity to CH_4 (S_{CH4}) obtained in numerical simulations with low space velocity (symbols) are compared to equilibrium values (lines). Parameters in numerical simulations: T_{int} = 550 K, T_f = 600 K, GHSV = 100 h^{-1}, $G_{MS} = G_{MS,0}$.

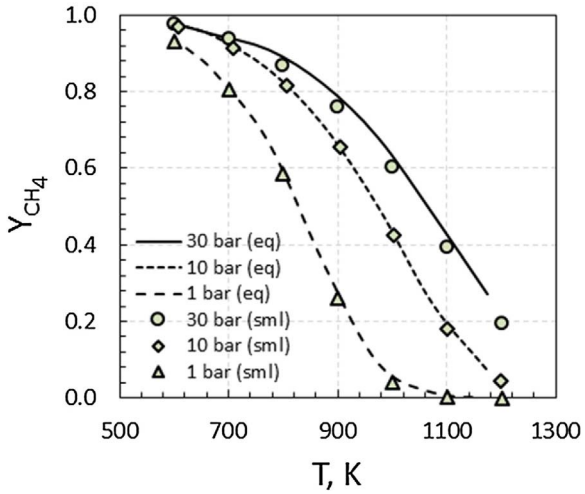

Fig. 4. Approach to equilibrium: CH_4 yield (Y_{CH4}) obtained in numerical simulations with low space velocity (symbols) as compared to equilibrium values (lines). Parameters in numerical simulations: T_{int} = 550 K, T_f = 600 K, GHSV = 100 h^{-1}, $G_{MS} = G_{MS,0}$.

not take place, similarly to the effect of preheating, Fig. 7. On the other hand, exceedingly high feed temperatures can result in reactor overheating, negatively affecting product distribution of the highly exothermic Sabatier reaction system, Eqs (1–3). In a practical situation, it is desirable to keep the feed temperature as low as possible to save energy. Another important consideration is feed temperature fluctuations which are unavoidable in real systems.

The effect of a step-wise change of the feed temperature is demonstrated in Fig. 8. For parameters listed in Fig. 8 and a feed temperature of T_f = 510 K, the simulation predicts formation of a stationary thermal front in the second half of the packed bed, left panels in Fig. 8 for t < 1 h. A step-wise increase of the feed temperature to T_f = 550 K immediately induces upstream front propagation with subsequent stabilization of the thermal front at the reactor entrance, Fig. 8a. If the feed temperature is abruptly decreased to T_f = 450 K, the front propagates downstream, eventually leading to the reactor extinction, Fig. 8b. Such moving thermal fronts are known to form in packed bed reactors with catalytic exothermic reactions; the propagation is due to the combine effect of heat generation, axial heat dispersion, and convection [27,28]. Understanding this phenomenon is important from the practical point of view, in order to avoid operating under conditions that can lead to the formation of downstream propagating thermal fronts that result in reactor extinction.

Ignition-extinction curves obtained by the gradual increase or decrease of the feed temperature are shown in Fig. 9, in terms of the maximum and outlet packed bed temperature as a function of the feed temperature. For low feed temperatures, which are below the ignition threshold, both the maximum and outlet temperatures increase linearly, until the ignition threshold of Tf > 500 K is reached. A small increase in the feed temperature beyond this threshold leads to reactor ignition, Fig. 9. Further increase in the feed temperature results in a moderate decrease of the maximum and outlet temperature, which can be attributed to the complex coupling of the reaction heat generation, inter-compartment heat transfer, and heat removal by the molten salt. When the feed temperature is gradually decreased following the top branch of the ignition-extinction curve, extinction occurs at T < 480 K.

Since the extinction temperature is different from the ignition threshold, there is a small region of bi-stability, where both the ignited and extinguished states co-exists. For practical applications, it is favorable to operate the reactor well outside the region of bi-stability where sudden reactor extinctions can occur as a result of fluctuations in the feed temperature. Fluctuations in operating parameters are expected to occur in real situations and other operating parameters can affect the extinction-ignition behavior as well, such as space velocity [27,28].

3.3.3. *Effect of space velocity*

Increasing space velocity is beneficial from the point of view of maximizing reactor throughput, even though it can negatively impact longevity. Nevertheless, it is important to understand the effect of increasing throughput on the reactor performance. In the analyzed reactor configuration (Fig. 2), the coupling of the reaction heat generation with the heat transfer between the compartments and heat removal by the molten salt can result in nontrivial behavior.

The effect of increasing space velocity on reactor profiles is demonstrated in Fig. 10, where elevated cooling rate was used ($G_{MS} = 0.5G_{MS,0}$). At low space velocity, Fig. 10a, the inter-compartment heat transfer is very efficient, resulting in equal temperatures in the packed bed and molten salt compartment, except for the small temperature difference at the reactor entrance, Fig. 10 (upper panel). For the parameters used in Fig. 10a, the simulation predicted highly efficient cooling. Both the gas stream and molten salt leave the reactor at the temperature which is only slightly higher than the molten salt feed temperature. Note, that heat losses to the environment was accounted for in the current study, last tram in Eq. (5).

Increasing the space velocity ten-folds leads to a very different distribution within the reactor, Fig. 10b. Though for the most of the reactor, the temperatures are equal in both compartments, a very

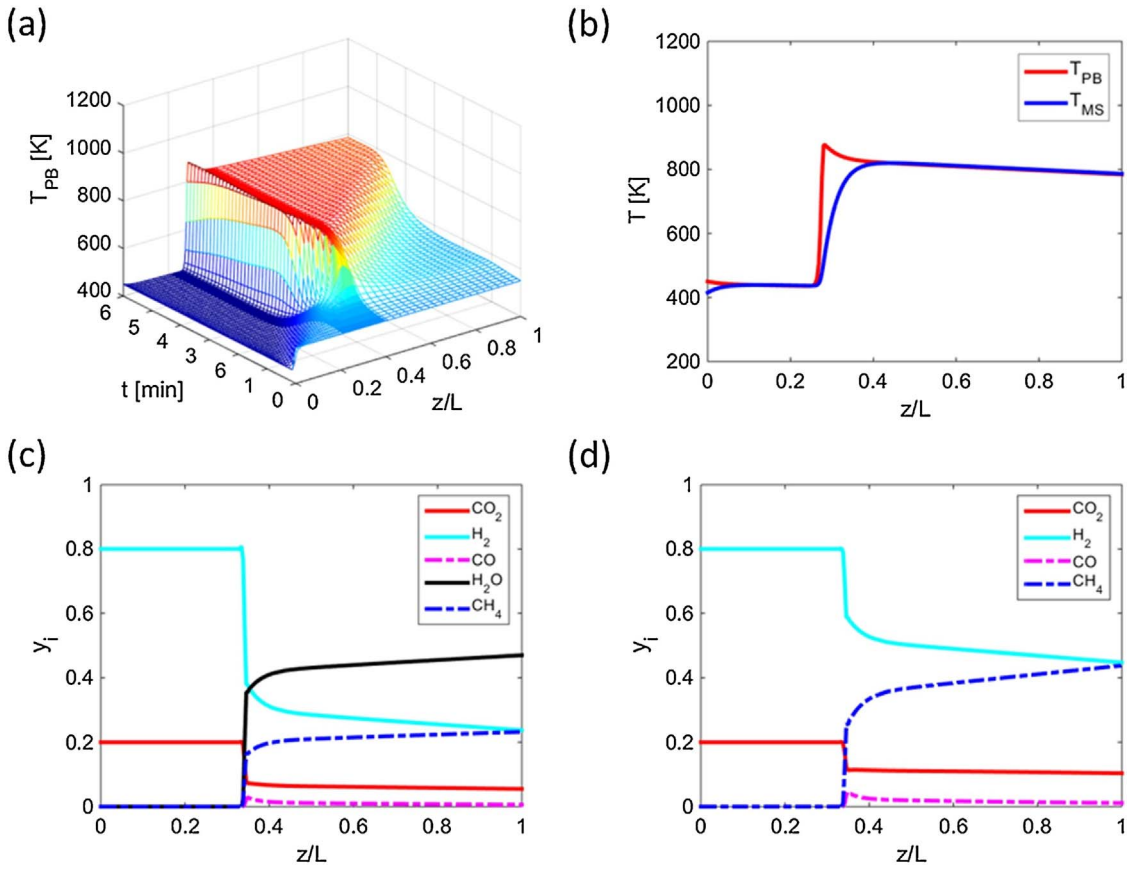

Fig. 5. The spatiotemporal profile of reactor ignition (a) and steady state spatial profiles of temperature (b), mole fractions (c), and mole fractions calculated on dry basis (d). T_{PB} and T_{MS} in upper panels denote temperatures in the packed bed (PB) and molten salt (MS) compartments, respectively; y_i denotes the mole fraction of a component i. Parameters in numerical simulations: $N_c = 22$, $T_{int} = 550$ K, $T_f = 450$ K, GHSV = 1000 h^{-1}, $G_{MS} = 0.1G_{MS,0}$.

significant temperature gradient exists in the first quarter of the reactor, upper panel in Fig. 10b. The cooling is much less efficient, though same ratio of $G_{MS} = 0.5G_{MS,0}$ is kept; the outlet temperature is ~600 K. The exceedingly high packed bed temperature at the reactor entrance affects the mole fraction distribution within the reactor. As a result of less efficient cooling, the outlet mole fraction of CH_4 is lower, lower panel in Fig. 10b. For high space velocities, the heat removal could be limited by the heat transfer between the compartments, which is represented in the model by the heat exchange terms, in Eqs. (5) and (6).

Wall heat transfer coefficients ($U_{w,HL}$, $U_{w,HE}$) are calculated from correlations, Eqs. (16)–(18), and, therefore, cannot be arbitrary manipulated. The reactor geometry is fixed in this study except for the number of cooling tubes (N_c) which can be varied within the restriction of the reactor design, Table 1. The effect of the number of coolant tubes on the reactor performance at high space velocity (GHSV = 10,000 h^{-1}) is demonstrated in Fig. 11. For $N_c = 22$, both streams (the reaction mixture and the coolant) exit the reactor at same temperature. Decreasing the number of cooling tubes leads to slightly lower outlet temperatures, until a significant difference between the outlet temperatures appear for $N_c < 12$. Though CO_2 conversion and CH_4 yield are not affected to a significant extent by the inefficient heat transfer, right panel in Fig. 11, the heat removal appears to be limited by the insufficient heat exchange area for $N_c < 12$. Note that the simulations predict CH_4 yields over 90% at the elevated space velocity of GHSV = 10,000 h^{-1}, Fig. 11.

As it is highly desirable to maximize the reactor throughput to increase the rate of CH_4 production and thus to reduce the capital cost investment, reactor performance should be investigated over the range of space velocities. In Fig. 12, the reactor performance is evaluated as a function of space velocity ranging from 1000 1/h to 25,000 1/h using $N_c = 13$, as reducing number of tubes will simplify reactor manufacturing and operation. Elevated rate of cooling was used, $G_{MS} = 0.4G_{MS,0}$, as previous simulations showed insufficient heat removal for $G_{MS} = 0.1G_{MS,0}$ (compare Fig. 6 and Fig. 10). The effect of the space velocity on the outlet CO_2 conversion, selectivity to CH_4, CH_4 yield is demonstrated in the left panel of Fig. 12; showing also the normalized pressure drop, $\Delta P_N = (P_f - P_{out})/P_f$. Corresponding outlet temperatures are shown on the right panel of Fig. 12.

For relatively low space velocities (GHSV < 5000 h^{-1}), outlet CO_2 conversions and CH_4 yields higher than 90% are predicted, while full selectivity to the formation of CH_4 is predicted at the reactor outlet. These results indicate that the cooling is sufficient to prevent the formation of CO. Indeed, as it can be seen from Fig. 12 (right panel), the outlet backed bed temperatures are below 700 K for GHSV < 5000 h^{-1}, for which the equilibrium predicts virtually no CO formation. Even though some CO can still be formed in the hottest part of the reactor, it is converted into CO_2 downstream.

As space velocity is further increased, the conversion and yield drop below 90% and the pressure drop starts to be significant, left panel of Fig. 12. The packed bed outlet temperature gradually increase, while the outlet molten salt temperature decreases. For GHSV > 7000 h^{-1}, there is a substantial difference between outlet temperatures, indicating insufficient heat removal due to the transport limitations, i.e., the rate of heat transfer through the walls of the cooling tubes is significantly lower than the rate of reaction heat generation. Importantly, the 80% CH_4 yield is still achieved at a high space velocity of GHSV = 15,000 h^{-1}, while the outlet molten salt temperature is well above the solidification point and below the thermal decomposition threshold; the operating range of the molten salt is 415–758 K [45]. Above the threshold of GHSV > 15,000 h^{-1}, the reactor performance

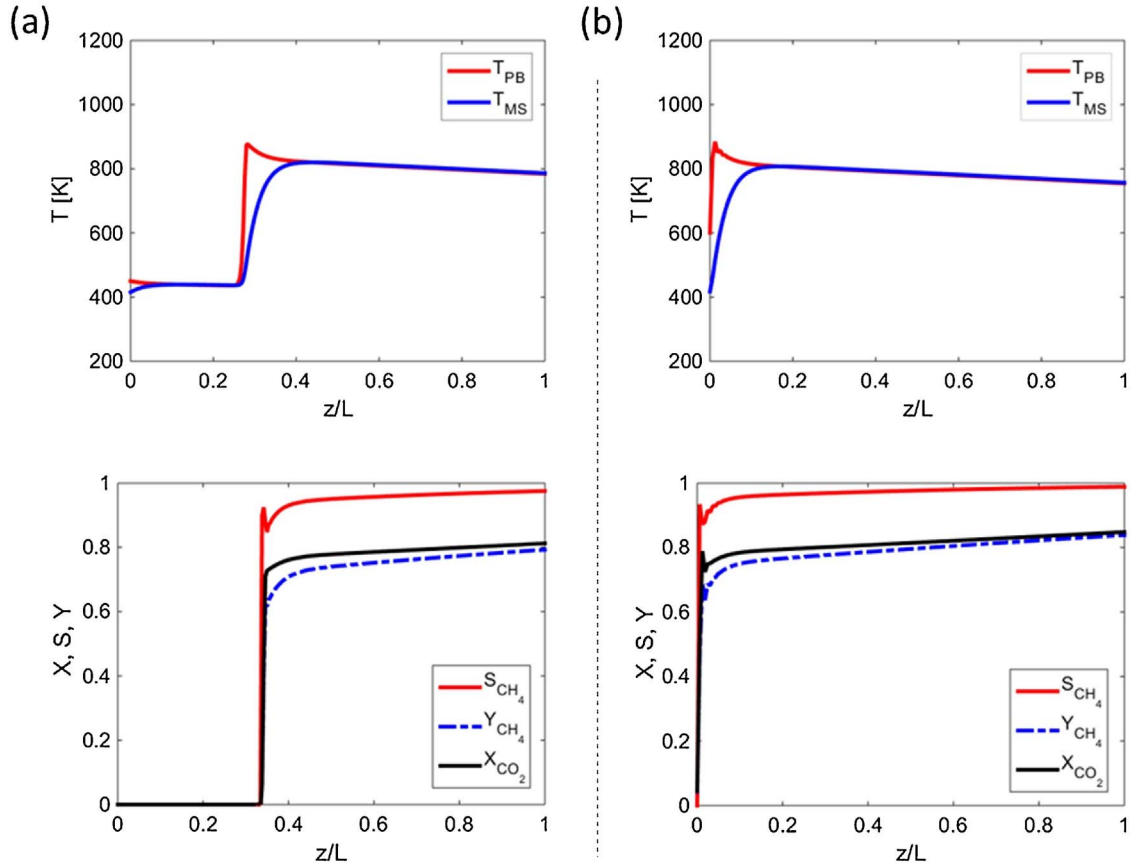

Fig. 6. Steady state spatial profiles of temperature (upper panels) and calculated reactor performance (lower panels) for gas stream feed temperatures of T_f = 450 K (a) and T_f = 600 K (b). T_{PB} and T_{MS} in upper panels) denote temperatures in the packed bed (PB) and molten salt (MS) compartments, respectively; X_{CO2}, S_{CH4}, and Y_{CH4} denote conversion, selectivity, and yield, Eqs. (19–21). Parameters in numerical simulations: N_c = 22, T_{int} = 550 K, GHSV = 1000 h^{-1}, $G_{MS} = 0.1G_{MS,0}$.

drops sharply, which can be attributed to overcooling. Note that the gas feed, which enters the reactor at a relatively low temperature of T_f = 600 K, also contributes to the cooling, especially at high space velocities. Pressure drop also increases considerably for GHSV > 15,000 h^{-1}, which can also contribute to the performance drop, as low pressures are thermodynamically unfavorable for the Sabatier reaction, Figs. 3 and 4. Note that in all simulations the inlet pressure was fixed to P_f = 500 kPa, Table 2.

3.3.4. Optimization of cooling rate

For process optimization, it is highly desirable to maximize the reactor throughput, while keeping high CH_4 yields. At the same time, the molten salt flow rate should be minimized in order to reduce energy investment in pumping and storage. However, decreasing the rate of cooling will lead to the increase of the reactor temperature reducing CO_2 conversion and, therefore, CH_4 production. Therefore, optimization of the molten salt flow rate, i.e., cooling rate, will be crucial for the reactor performance improvement and, therefore, for system optimization.

Effect of the cooling rate on the reactor performance is first examined for a fixed space velocity, Fig. 13. For low cooling rate of $G_{MS} = 0.1G_{MS,0}$, Fig. 13a, the heat removal is insufficient and CO_2 is

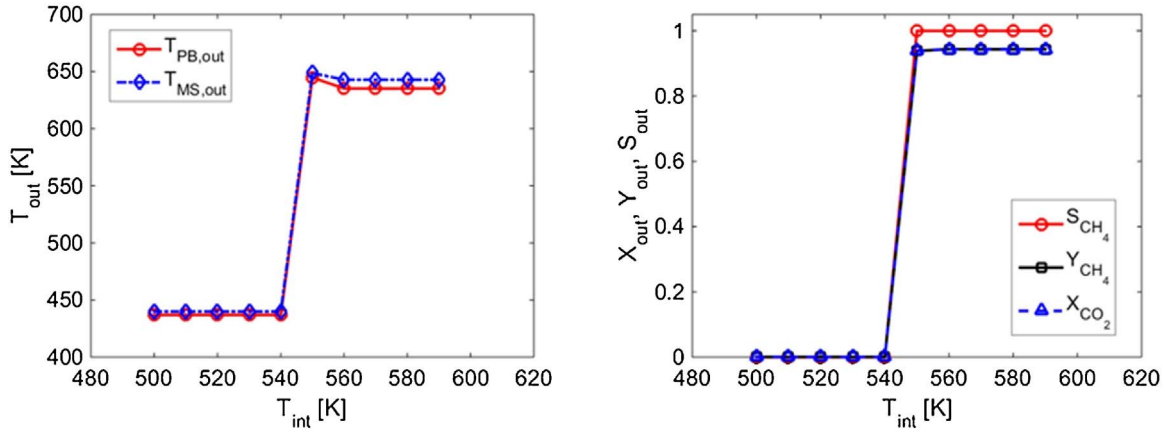

Fig. 7. Effect of the initial reactor temperature (pre-heating, start-up temperature) on the steady state reactor performance in terms of the outlet temperature (left panel) and outlet conversion, selectivity, and yield (right panel). Parameters: N_c = 13, T_f = 520 K, GHSV = 1000 h^{-1}, $G_{MS} = 0.38G_{MS,0}$.

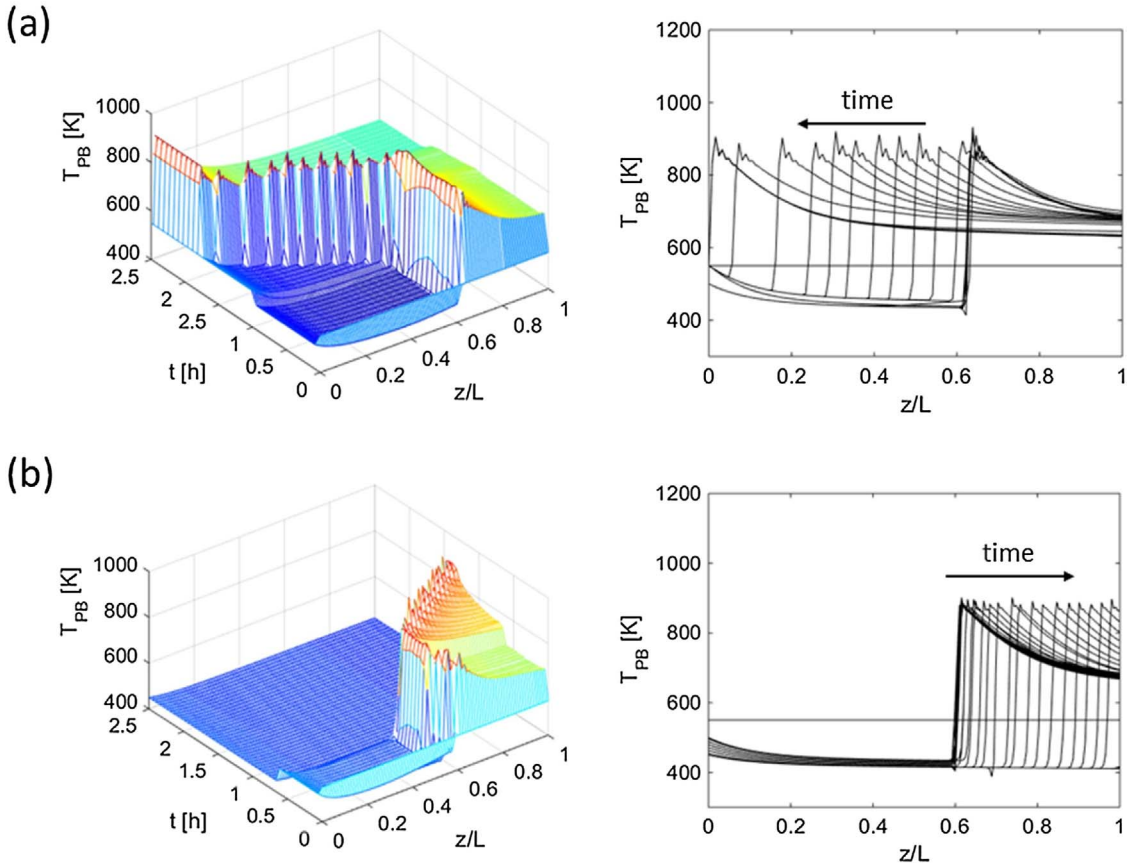

Fig. 8. Moving thermal fronts propagating upstream (a), as a result of increasing feed temperature from T_f = 510 K to T_f = 550 K, and downstream (b), as a result of switching feed temperature from T_f = 510 K to T_f = 450 K. Right panels show 2D representation of the spatio-temporal 3D patterns shown in left panels. Parameters: N_c = 13, T_{int} = 550 K, GHSV = 1000 h^{-1}, $G_{MS} = 0.38G_{MS,0}$.

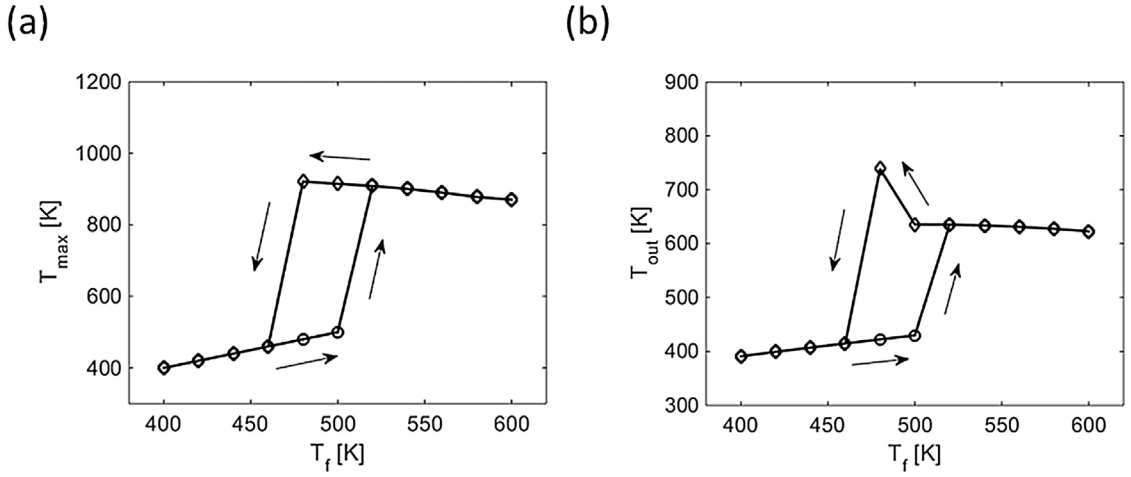

Fig. 9. Ignition-extinction curves showing the packed bed maximum temperature (a) and the packed bed outlet temperature (b) as a function of the gas feed temperature. All results shown were obtained after the steady state was achieved. Parameters: N_c = 13, T_{int} = 550 K, GHSV = 1000 h, G_{MS} = .

only consumed at the reactor entrance. There is further consumption of H_2 downstream the reactor, but only due to the CO conversion, lower panel of Fig. 13a. Importantly, the molten salt temperature is above 800 K for the most of the reactor, which is outside the operating range and thus will lead to thermal decomposition of the molten salt. Increasing the cooling rate ten-fold, to $G_{MS} = G_{MS,0}$, changes reactor profiles dramatically, Fig. 13b. The molten salt temperature is within its operating range, upper panel in Fig. 13b and the packed bed temperature is cooled down along the reactor. As a result, in addition to the CO_2 consumption at the reactor entrance, there is additional CO_2 consumption downstream the reactor, resulting in a dramatic improvement of CH_4 production, lower panel in Fig. 13b. Once can conclude that a declining temperature profile is highly favorable for CH_4 production via Sabatier reaction. From the thermodynamic point of view, relatively high temperatures in the first part of the packed bed favor CO_2 conversion into CH_4 but also to CO, Fig. 3. As temperature declines downstream the reactor, the CO formed is converted into more CH_4, as it is predicted by the equilibrium, Fig. 3.

The reactor performance for low and high cooling rates is analyzed in Fig. 14 over a wide range of space velocities, in terms of outlet

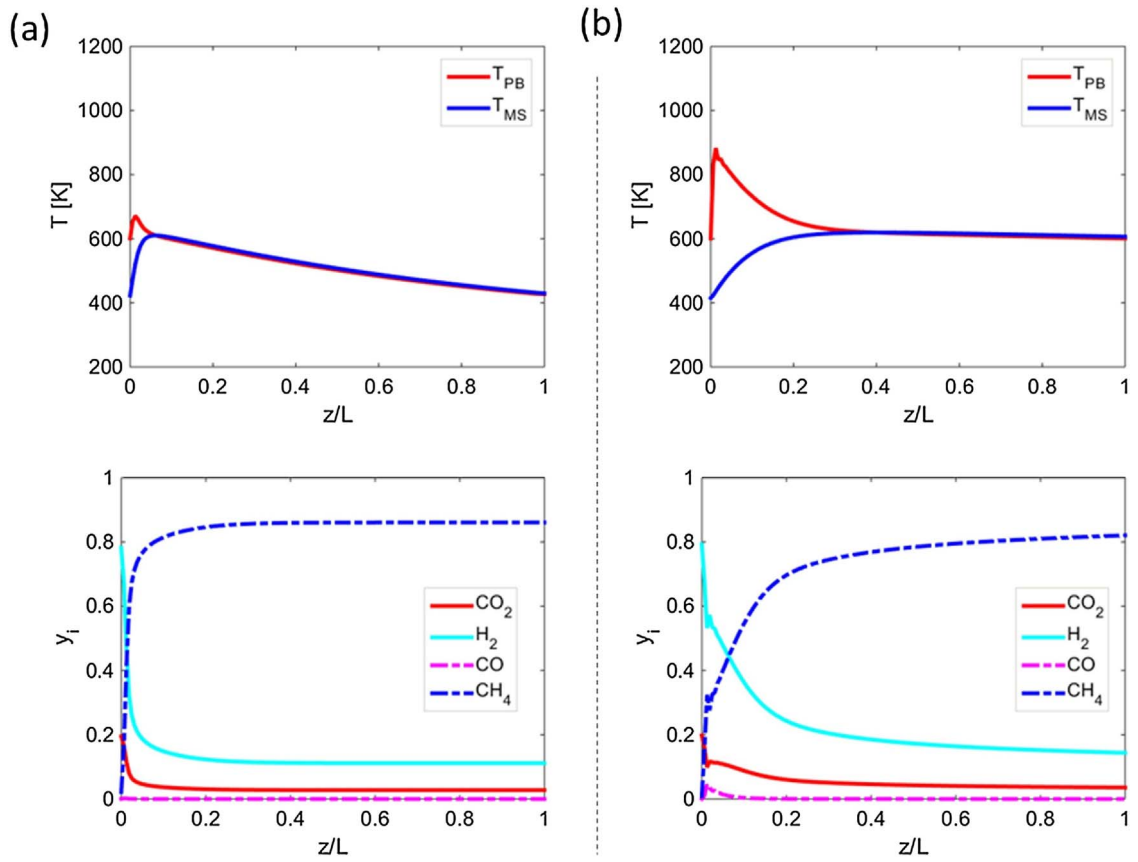

Fig. 10. Stationary temperature profiles (upper panels) and mole fraction distributions (lower panels) for low space velocity, GHSV = 100 h^{-1} (a) and for elevated space velocity, GHSV = 1000 h^{-1} (b). Parameters: N_c = 22, T_{int} = 550 K, T_f = 600 K, $G_{MS} = 0.5G_{MS,0}$.

conversion, selectivity, and yield (also showing pressure drop). From analyzing Fig. 14 in comparison with Fig. 12 (intermediate cooling rate), one can conclude that the sharp drop in the reactor performance can be rather attributed to overcooling by the molten salt. As the cooling rate is increased from low ($G_{MS} = 0.08G_{MS,0}$, left panel in Fig. 14) to intermediate ($G_{MS} = 0.38G_{MS,0}$, left panel in Fig. 12), and to high ($G_{MS} = 0.77G_{MS,0}$, right panel in Fig. 14), the performance drop threshold decreases from GHSV = 36,000 h^{-1}, to GHSV = 15,000 h^{-1}, and GHSV = 8000 h^{-1}.

Pressure drop can also contribute to the drop in performance, particularly for the case of the low cooling rate: the pressure drop becomes very significant at the threshold space velocity of GHSV = 36,000 h^{-1} (Fig. 14, left panel). Since CH_4 production is favored by high pressures (Figs. 3, 4), it is desirable to keep the entire reactor at high pressure. Operation at low cooling rate is also disadvantageous from the point of view of conversion and selectivity. High conversion and selectivity are only attainable for low space velocity. As the space velocity is increased, both CO_2 conversion and selectivity to CH_4 drop significantly, resulting in CH_4 yields below 60%. This can be attributed to insufficient cooling that results in exceedingly high temperatures that suppress CH_4 production. Overcooling, i.e. high cooling rate (Fig. 14, right panel) is also disadvantages. Though high CH_4 yield is obtained, operation is limited to GHSV < 10,000 h^{-1}.

Since the reactor performance is strongly affected by the rate of heat

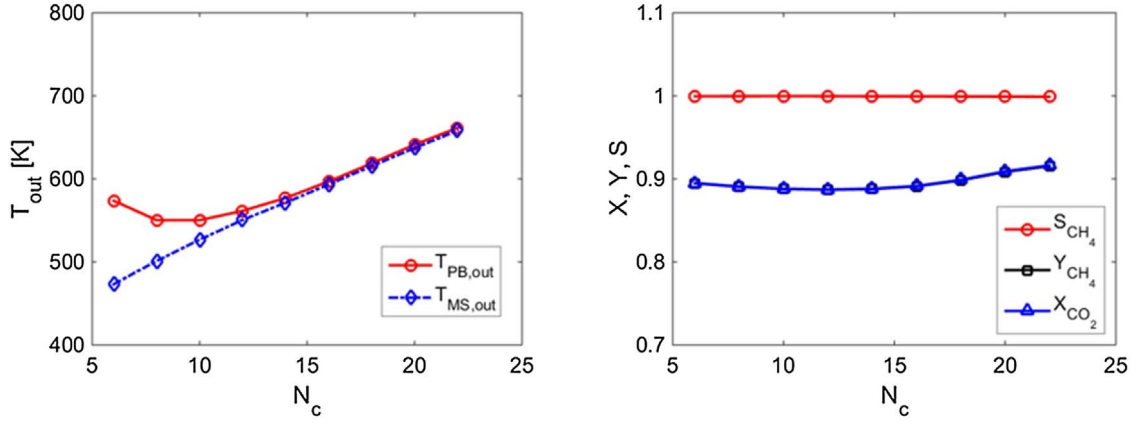

Fig. 11. Effect of the number of cooling tubes on the steady state reactor performance at high space velocity. Outlet temperatures of the packed bed (PB) and coolant, molten salt (MS) compartments (a) and outlet conversion, selectivity, and yield (b) are plotted versus the number of cooling tubes (N_c) in the reactor. Parameters: T_{int} = 550 K, T_f = 650 K, GHSV = 10,000 h^{-1}, $G_{MS} = G_{MS,0}$.

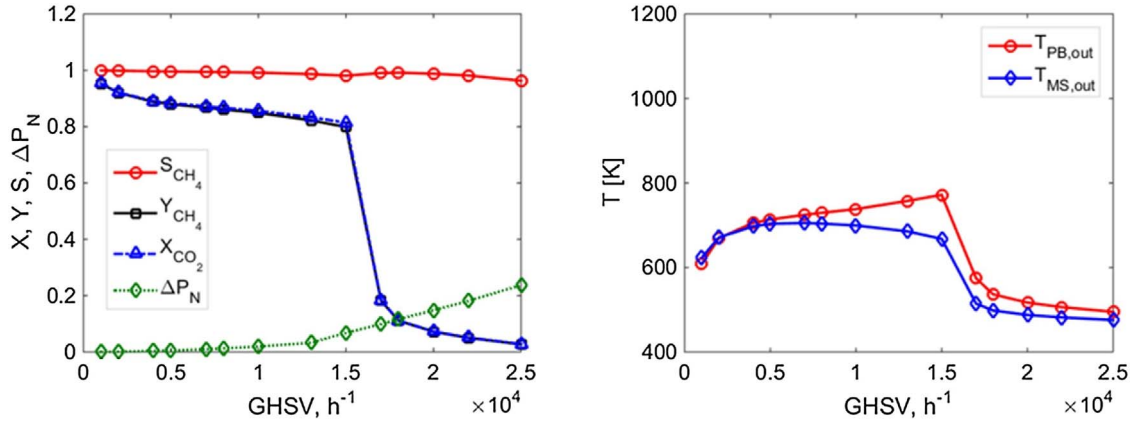

Fig. 12. Effect of space velocity on the steady state reactor performance. Outlet conversion, selectivity, and yield, and normalized pressure drop (left panel) and outlet temperatures in the packed bed and molten salt compartments (right panel) are plotted versus gas space velocity. Normalized pressure drop is defined as $\Delta P_N = (P_f - P_{out})/P_f$. Parameters: $N_c = 13$, $T_{int} = 550$ K, $T_f = 600$ K, $G_{MS} = 0.38 G_{MS,0}$.

removal, cooling rate optimization is of crucial importance. The effect of the cooling rate at high (fixed) space velocities is examined in Fig. 15. Outlet conversion, selectivity, and yield are plotted versus the molten salt flow rate for GHSV = 20,000 h^{-1} (Fig. 15a) and GHSV = 45,000 h^{-1} (Fig. 15b). The increase in the molten salt gravimetric flow rate initially leads to a considerable improvement in CH_4 production, which is followed by a sharp drop after a certain threshold, similarly to the effect of space velocity, Figs. 12, 14. While for GHSV = 20,000 h^{-1} the selectivity to CH_4 remains almost complete over the entire range, GHSV = 45,000 h^{-1} increasing the molten salt flow rate results in a very significant improvement, right panel in Fig. 15. In both cases, the optimum in the CH_4 yield is observed, more pronounced for the higher space velocity. Also, the sharp drop in the reactor performance occurs at a lower $G_{MS}/G_{MS,0}$ ratio for GHSV = 45,000 h^{-1}.

To summarize the findings discussed in two last sub-sections, it can be concluded that both space velocity and cooling rate (molten slat flow rate) are crucial parameters affecting the reactor performance. The (desirable) increase in the space velocity unavoidably leads to the declining CH_4 yield and, eventually, a threshold-like drop in performance leading to conversions and yields which cannot be considered practical (below 20%). Moderately elevated (GHSV < 10,000 h^{-1}) space velocities with intermediate cooling rates ($G_{MS} \approx 0.5 G_{MS,0}$) are recommended for the reactor configuration analyzed here.

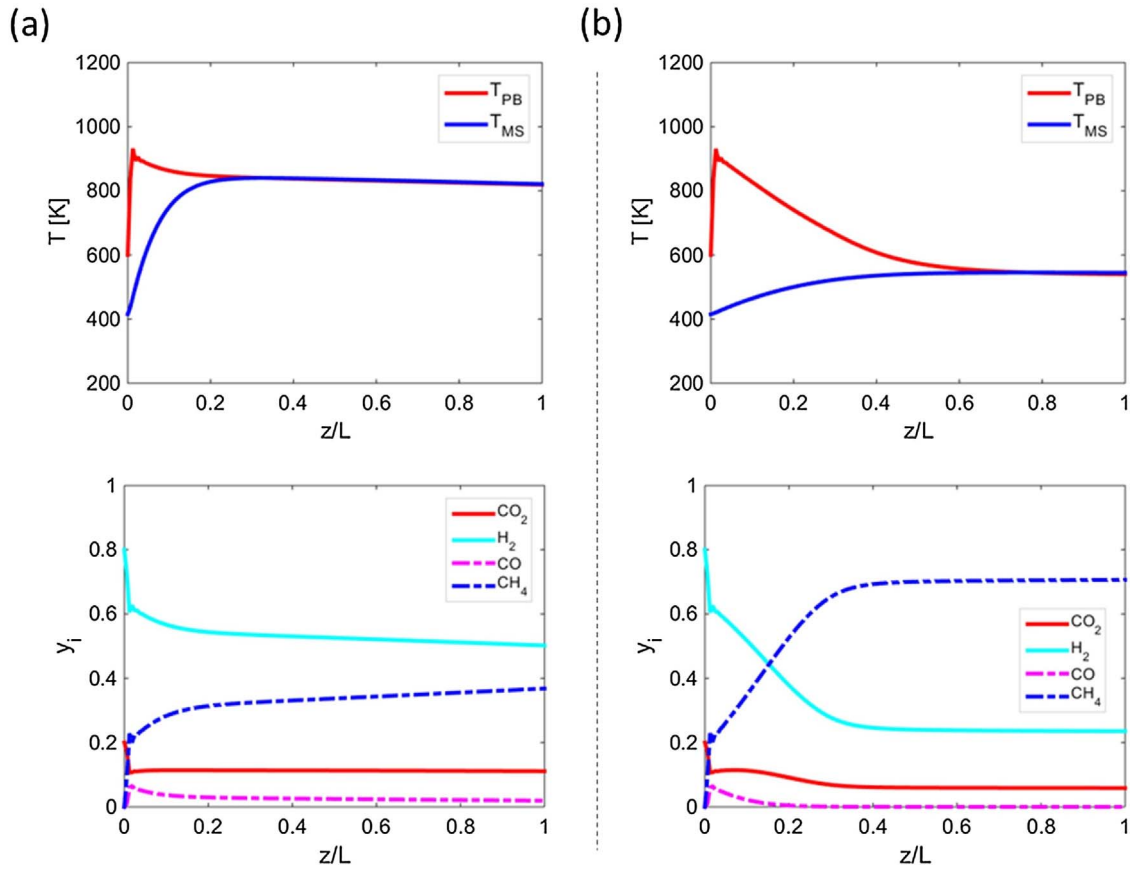

Fig. 13. Effect of the cooling rate on the reactor performance. Stationary temperature profiles (upper panels) and mole fraction distributions (lower panels) are shown for the relatively low cooling rate, $G_{MS} = 0.1 G_{MS,0}$ (a), and for the elevated cooling rate, $G_{MS} = G_{MS,0}$ (b). Parameters: $N_c = 22$, $T_{int} = 550$ K, $T_f = 600$ K, GHSV = 2000 h^{-1}.

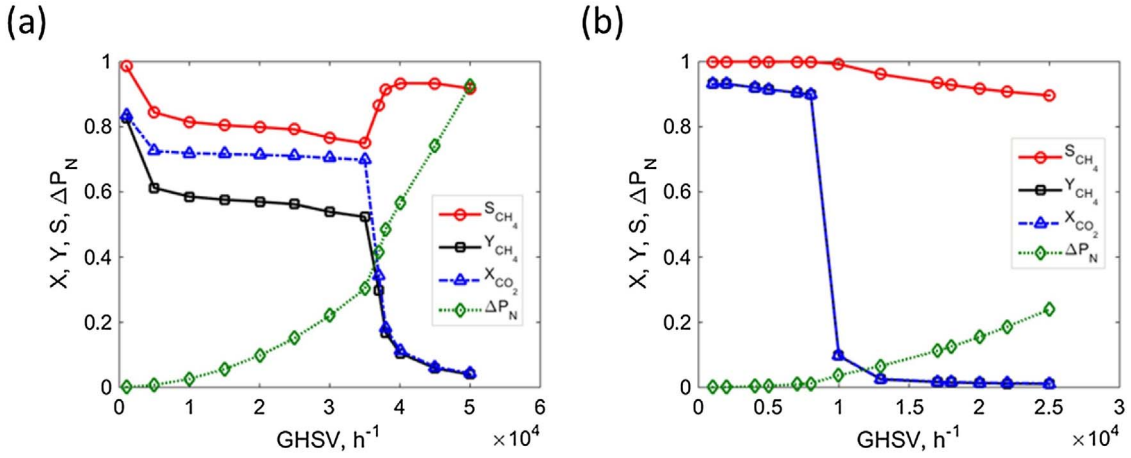

Fig. 14. Effect of the heat removal rate on the steady state reactor performance. Outlet conversion, selectivity, yield, and normalized pressure drop are plotted versus space velocity for relatively low cooling rate, $G_{MS} = 0.08G_{MS,0}$ (a) and elevated cooling rate, $G_{MS} = 0.77G_{MS,0}$ (b). Parameters: $N_c = 13$, $T_{int} = 550$ K, $T_f = 600$ K.

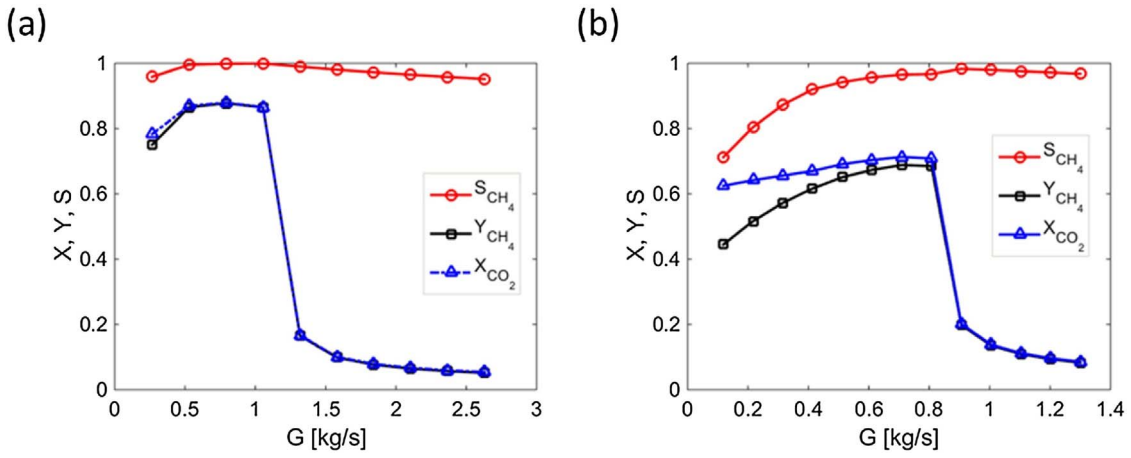

Fig. 15. Effect of the cooling rate on the steady state reactor performance at high space velocities. Outlet conversion, selectivity, and yield are plotted versus the molten salt flow rate for GHSV = 20,000 h^{-1} (a) and GHSV = 45,000 h^{-1} (b). Ranges of the molten salt flow rate correspond to $G_{MS} = (0.2\text{-}2.3)G_{MS,0}$ (a) and $G_{MS} = (0.05\text{-}0.4)G_{MS,0}$ (b). Parameters: $N_c = 13$, $T_{int} = 550$ K, $T_f = 650$ K.

3.4. Preliminary techno-economic evaluation

For practical applications, the Sabatier reactor analyzed in this study should be eventually incorporated into the entire renewable natural gas (RNG) production system represented in Fig. 1. Such a system can be used for converting waste streams containing significant amounts of CO_2 into RNG which can be injected into the existing natural gas infrastructure. Suitable feedstocks include combustion flue gases, as well as biogas and landfill gas. Biogas and landfill gas already contain a significant fraction of non-fossil CH_4 (up to 60%) and can be, therefore, directly used for power generation via combustion. However, this approach has low efficiency due to the thermodynamic limitations

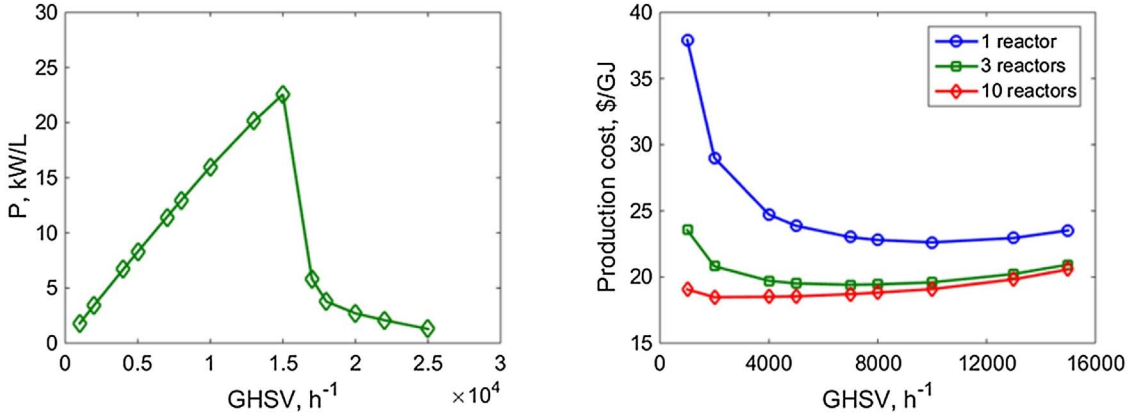

Fig. 16. Techno-economic evaluation in terms of the reactor power density, Eq. (24), and the renewable natural gas production cost, Eq. (25), as a function of the reactor throughput. The production cost (right panel) is shown for a single reactor, three reactors, and 10 reactors, for the cumulative 10,000 h of operation. Parameters: $N_c = 13$, $T_{int} = 550$ K, $T_f = 600$ K, $G_{MS} = 0.38G_{MS,0}$.

of combustion engines. Alternatively, these feedstocks can be upgraded into RNG via pre-separation of CH_4 (can be directly used as RNG) and converting the remaining CO_2 into more renewable methane.

This approach has a potential to provide enormous storage and transportation capacities for the re-distribution of renewable energy. Renewable sources such as solar and wind energy are abundant but their efficient utilization is challenging due to its transient nature resulting in the supply-demand mismatch. Fluctuations in power supply can be compensated by storing off-peak power in batteries but this approach has limitations of energy density, cost, and scalability. An alternative route is to store the surplus electricity in the form of chemical energy of the RNG. However, in order to assess the economic viability of this approach, the production cost of the resulted RNG should be estimated.

Herein, we provide only a preliminary techno-economic evaluation by integrating the reactor analyzed in this study into the entire system, Fig. 1. One of the important considerations is the reactor compactness, which can be evaluated by calculating the power density as a function of the reactor throughput (LHV stands for low heating value):

$$P = \frac{F_{CH_4,out} LHV_{CH_4}}{V_r} \tag{24}$$

The calculated power densities shown in Fig. 16 (left panel) correspond to the results presented in Fig. 12. The power density increases nearly linearly for increasing reactor throughputs, as the rate of CH_4 production increases, for the fixed reactor size. Very high power density is achieved at the optimum, before the reactor performance declines sharply, resulting in a drop of CH_4 production.

To evaluate CH_4 production cost, we consider the most essential elements of the synthetic methane generation system shown in Fig. 1: a molten salt pump, a steam turbine, and the reactor itself. The H_2 production infrastructure cost is lumped in the price of H_2. It is assumed that a pure stream of CO_2 is available. The production cost was calculated using the following equation:

$$\begin{aligned} &production\ \ cost = capital\ \ investement + pumping\ \ cost \times t + \\ &+ [F_{H_2,f} \times H_2\ price - \eta_{ST} G_{MS} C_{P,MS} (T_{MS,out} - T_{MS,f}) \times electricity\ \ price] \\ &\times t \end{aligned} \tag{25}$$

The capital investment includes the cost of the reactor, molten salt pump, and steam turbine. The reactor cost will not be a significant contribution, since the price of Ni-based catalysts considered in our study is relatively low and the reactor construction material is also low-cost (stainless steel). A typical price of Ni-based catalysts is 50 $/kg (e.g., Johnson Matthey). The packed bed volume is ~ 25 L, which will result in approximately $3000 cost of a single reactor (including $1500 catalyst cost and manufacturing). The molten salt pump and steam turbine costs were assumed to be $40,000 and $58,000, respectively; these are typical prices for the small-to-medium scale equipment (e.g., [47,48]). The electricity consumption for pumping is considered in Eq. (25) as well, but this contribution was found to be rather insignificant to another time-dependent cost which is H_2 consumption. A (rather optimistic) projection of 2 $/kg was used as a price of renewable H_2. The cost of H_2 consumed can be partially recovered by electricity generation by a steam turbine, Fig. 1, using the reactor outlet molten salt to generate steam. The overall efficiency of the electricity generation from the molten salt heat (η_{ST}) was assumed to be 30% and the electricity celling price was fixed to 0.13 $/kWh. Labor, maintenance, and equipment replacement/depreciation costs were not included in our preliminary assessment.

The production cost calculated using Eq. (25) (right panel in Fig. 16) clearly cannot compete with the current low prices of natural gas (~2.5 $/GJ), although historically the price of natural gas fluctuated well above 10 $/GJ (in 2008). Also, the process analyzed in this study consumes CO_2, which can be potentially used for carbon trading. Even though the produced renewable natural gas (RNG) will be eventually burned to generate electricity and heat, the use of RNG reduces the consumption of the fossil natural gas, reducing therefore CO_2 emissions. This is in particular true if the source of CO_2 is not fossil, such as fermentation flue gas or biogas.

As it can be seen from Fig. 16, increasing the number of reactors reduces the production cost substantially. For the relatively small reactor size analyzed herein, no additional molten salt pump or steam turbine is required up to ten reactors, and the cost of reactors is low. As a result, when the number of reactors is increased, the capital cost remains almost same, reducing the production cost. For a small number of reactors, it is beneficial to operate at high space velocities. For ten reactors, similar price is obtained over the entire range, though there is a slight optimum for moderately high space velocity.

Importantly, the production cost drops down below 20 $/GJ, starting to approach the price of H_2: 2 $/kg is equivalent to 16.6 $/GJ for H_2, using the low heating value. From the thermodynamic point of view, the maximum of 83% of the H_2 energy content can be recovered via the Sabatier reaction (low heating values of CH_4 and H_2 are 802.3 KJ/mol and 241.8 kJ/mol, respectively); the rest is dissipated as heat, Eq. (1). In this case, the CH_4 production cost will be ~20 $/GJ. Because some heat is recovered from the molten salt stream for electricity generation, Fig. 1, Eq. (25), it is possible to reduce the production cost even below 20 $/GJ even for incomplete CO_2 conversion and CH_4 yield.

Note that the relatively low calculated RNG production cost is mainly a derivative of the assumed low H_2 production cost of 2 $/kg. However, this cost coincides with the cost goal set by the US Department of Energy (2–3 $/kg) [49] and might be provided in the future by novel technologies such as high temperature water splitting [50]. Another source of the estimated low RNG cost is the use of the compact, high power density reactor units placed in parallel. This configuration is different from the more conventional multiple reactor configuration with inter-stage cooling that would require much higher capital investment and operating costs, contributing to significantly higher production costs [51]. Some post-purification might be also required for the outlet stream depending on application, increasing the RNG production cost. Nevertheless, the lower limit of 20 $/GJ estimated in our study coincides with some lower limit estimations reported in the public domain [52–54] and some recent studies on the techno-economic evaluation and life-cycle analysis of CO_2 methanation systems (25–40 $/GJ) [55]. It should be mention that other studies provide much higher estimates (30–120 $/GJ) [26].

4. Concluding remarks

The molten salt-cooled heat exchanger type packed bed reactor was suggested as a novel design configuration for synthetic methane production via Sabatier reaction. A mathematical model was defined and analyzed using numerical simulations in order to determine the effects of operating parameters and to find optimal operation regimes. The reactor performance was evaluated in terms of CO_2 conversion and CH_4 yield, as a function of various parameters including feed temperature, space velocity and cooling rate, which were found to be of crucial importance for the reactor performance. The simulations predicted that under certain optimized operating conditions it is possible to obtain CH4 yields of more than 90% at elevated, industrially relevant space velocities.

Optimizing the rate of cooling, i.e. the molten salt flow rate, is a challenging task. On one hand, high cooling rates produce a declining temperature profile in the packed bed which is beneficial from the thermodynamic point of few: low temperatures facilitate methane formation in the exothermic Sabatier reaction. On the other hand, overcooling can lead to a sharp performance drop and even to reactor extinction. Low cooling rates should be avoided because they result in exceedingly high temperatures that negatively affect CH_4 formation and can lead, in a practical situation, to the thermal decomposition of the

molten salt. Increasing space velocity is beneficial from the point of view of increased reactor throughputs and, therefore, higher rate of CH_4 production. However, high space velocities can lead to reactor extinction in a threshold-like manner similar to the effect of the overcooling by molten salt.

A preliminary techno-economic evaluation carried out at the system level predicted the production cost of the renewable natural gas (RNG) below 20 $/GJ, for multiple reactors and the optimized cooling rate and reactor throughput. The most significant contribution to the RNG production cost is expected to be the price of renewable H_2. Therefore, reducing the production cost of renewable H_2 can lead to a widespread introduction of RNG into the markets. Importantly, most of the energy content of H_2 consumed in the reaction is recovered in the RNG produced and electricity co-generated (up to 80%). Since renewable H_2 produced in a distributed manner is less suitable for storage and transportation, converting this renewable H_2 into RNG could be an attractive avenue for storage and re-distribution of the transient renewable sources such as solar and wind energy.

Acknowledgement

The authors acknowledge the support of the Waterloo Institute of Sustainable Energy (WISE) through the WISE – Cisco Systems Smart Grid Research Fund.

References

[1] B. Kumar, M. Llorente, J. Froehlich, T. Dang, A. Sathrum, C.P. Kubiak, Photochemical and photoelectrochemical reduction of CO_2, Annu. Rev. Phys. Chem. 63 (2012) 541–569.
[2] Y. Chen, N.S. Lewis, C. Xiang, Operational constraints and strategies for systems to effect the sustainable, solar-driven reduction of atmospheric CO_2, Energy Environ. Sci. 8 (2015) 3663–3674.
[3] W. Wang, S. Wang, X. Ma, J. Gong, Recent advances in catalytic hydrogenation of carbon dioxide, Chem. Soc. Rev. 40 (2011) 3703–3727.
[4] W. Wang, J. Gong, Methanation of carbon dioxide: an overview, Front. Chem. Sci. Eng. 5 (2011) 2–10.
[5] T. Schaaf, J. Grünig, M.R. Schuster, T. Rothenfluh, A. Orth, Methanation of CO_2 – storage of renewable energy in a gas distribution system, Energy Sustain Soc. 4 (2014).
[6] J. Kopyscinski, T.J. Schildhauer, S.M.A. Biollaz, Production of synthetic natural gas (SNG) from coal and dry biomass – a technology review from 1950 to 2009, Fuel 89 (2010) 1763–1783.
[7] Y.-L. Kao, P.-H. Lee, Y.-T. Tseng, I.L. Chien, J.D. Ward, Design, control and comparison of fixed-bed methanation reactor systems for the production of substitute natural gas, J. Taiwan Inst. Chem. Eng. 45 (2014) 2346–2357.
[8] I. Kiendl, M. Klemm, A. Clemens, A. Herrman, Dilute gas methanation of synthesis gas from biomass gasification, Fuel 123 (2014) 211–217.
[9] D. Schlereth, O. Hinrichsen, A fixed-bed reactor modeling study on the methanation of CO_2, Chem. Eng. Res. Des. 92 (2014) 702–712.
[10] L. Kiewidt, J. Thöming, Predicting optimal temperature profiles in single-stage fixed-bed reactors for CO_2-methanation, Chem. Eng. Sci. 132 (2015) 59–71.
[11] B. Hou, Y. Huang, X. Wang, X. Yang, H. Duan, T. Zhang, Optimization and simulation of the Sabatier reaction process in a packed bed, AIChE J. 62 (2016) 2879–2892.
[12] M.C. Seemann, T.J. Schildhauer, S.M. Biollaz, Fluidized bed methanation of wood-derived producer gas for the production of synthetic natural gas, Ind. Eng. Chem. Res. 49 (2010) 7034–7038.
[13] J. Li, L. Zhou, P. Li, Q. Zhu, J. Gao, F. Gu, F. Su, Enhanced fluidized bed methanation over a Ni/Al2O3 catalyst for production of synthetic natural gas, Chem. Eng. J. 219 (2013) 183–189.
[14] J. Kopyscinski, T.J. Schildhauer, S.M.A. Biollaz, Methanation in a fluidized bed reactor with high initial CO partial pressure: part I—experimental investigation of hydrodynamics, mass transfer effects, and carbon deposition, Chem. Eng. Sci. 66 (2011) 924–934.
[15] K.P. Brooks, J. Hu, H. Zhu, R.J. Kee, Methanation of carbon dioxide by hydrogen reduction using the Sabatier process in microchannel reactors, Chem. Eng. Sci. 62 (2007) 1161–1170.
[16] M. Sudiro, A. Bertucco, G. Groppi, E. Tronconi, Simulation of a structured catalytic reactor for exothermic methanation reactions producing synthetic natural gas, Comput. Aided Chem. Eng. 28 (2010) 691–696.
[17] C. Junaedi, K. Hawley, D. Walsh, S. Roychoudhury, CO_2 reduction assembly prototype using microlith-based Sabatier reactor for ground demonstration, 44th International Conference on Environmental Systems (2014).
[18] C. Junaedi, K. Hawley, S.A. Vilekar, S. Roychoudhury, Evaluation of CO_2 adsorber, Sabatier reactor, and solid oxide stack for consumable, propellant, and power production – potential in ISRU architecture, 46th International Conference on Environmental Systems (2016).
[19] M. Götz, F. Ortloff, R. Reimert, O. Basha, B.I. Morsi, T. Kolb, Evaluation of organic and iIonic liquids for three-phase methanation and biogas purification processes, Energy Fuel 27 (2013) 4705–4716.
[20] J. Lefebvre, M. Götz, S. Bajohr, R. Reimert, T. Kolb, Improvement of three-phase methanation reactor performance for steady-state and transient operation, Fuel Process. Technol. 132 (2015) 83–90.
[21] S. Rönsch, J. Schneider, S. Matthischke, M. Schlüter, M. Götz, J. Lefebvre, P. Prabhakaran, S. Bajohr, Review on methanation – From fundamentals to current projects, Fuel 166 (2016) 276–296.
[22] S.A.M. Said, D.S.A. Simakov, M. Waseeuddin, Y. Roman-Leshkov, Solar molten salt heated membrane reformer for natural gas upgrading and hydrogen generation: a CFD model, Sol. Energy 124 (2016) 163–176.
[23] S.A.M. Said, M. Waseeuddin, D.S.A. Simakov, A review on solar reforming systems, Renewable Sustainable Energy Rev. 59 (2016) 149–159.
[24] D.S.A. Simakov, M.M. Wright, S. Ahmed, E.M.A. Mokheimer, Y. Román-Leshkov, Solar thermal catalytic reforming of natural gas: a review on chemistry, catalysis and system design, Catal. Sci. Technol. 5 (2015) 1991–2016.
[25] G. Gahleitner, Hydrogen from renewable electricity: an international review of power-to-gas pilot plants for stationary applications, Int. J. Hydrogen Energy 38 (2013) 2039–2061.
[26] M. Götz, J. Lefebvre, F. Mörs, A. McDaniel Koch, F. Graf, S. Bajohr, R. Reimert, T. Kolb, Renewable power-to-gas: a technological and economic review, Renew. Energy 85 (2016) 1371–1390.
[27] D.S.A. Simakov, M. Sheintuch, Design of a thermally balanced membrane reformer for hydrogen production, AIChE J. 54 (2008) 2735–2750.
[28] D.S.A. Simakov, M. Sheintuch, Model-based optimization of hydrogen generation by methane steam reforming in autothermal packed-bed membrane reformer, AIChE J. 57 (2011) 525–541.
[29] R. Güttel, Study of unsteady-state operation of methanation by modeling and simulation, Chem. Eng. Technol. 36 (2013) 1675–1682.
[30] J. Xu, G.F. Froment, Methane steam reforming, methanation and water-gas shift: I. Intrinsic kinetics, AIChE J. 35 (1989) 88–96.
[31] S.S.E.H. Elnashaie, A.M. Adris, A.S. Al-Ubaid, M.A. Soliman, On the non-monotonic behaviour of methane steam reforming kinetics, Chem. Eng. Sci. 45 (1990) 491–501.
[32] M.L. Rodríguez, M.N. Pedernera, D.O. Borio, Two dimensional modeling of a membrane reactor for ATR of methane, Catal. Today 193 (2012) 137–144.
[33] G.F. Froment, K.B. Bischoff, Chemical Reactor Analysis and Design, Wiley, New York, 1979.
[34] R.J. Berger, J. Pérez-Ramírez, F. Kapteijn, A. Moulijn, Catalyst performance testing: radial and axial dispersion related to dilution in fixed-bed laboratory reactors, Appl. Catal. A Gen. 227 (2002) 321–333.
[35] A.G. Dixon, D.L. Cresswell, Theoretical prediction of effective heat transfer parameters in packed beds, AIChE J. 25 (1979) 663–676.
[36] O.R. Derkx, A.G. Dixon, Effect of the wall Nusselt number on the simulation of catalytic fixed bed reactors, Catal. Today 35 (1997) 435–442.
[37] O.A. Sergeev, A.G. Shashkov, A.S. Umanskii, Thermophysical properties of quartz glass, J. Eng. Phys. Thermophys. 43 (1982) 1375–1383.
[38] S.W. Churchill, H.H. Chu, Correlating equations for laminar and turbulent free convection from a horizontal cylinder, Int. J. Heat Mass Transfer 18 (1975) 1049–1053.
[39] A.F. Mills, Heat Transfer, 2nd ed., Prentice-Hall, New Jersey, 1999.
[40] V. Gnielinski, New equations for heat and mass transfer in turbulent pipe and channel flow, Int. Chem. Eng. 16 (1976) 359–368.
[41] J.P. Holman, Heat Transfer, 9th ed., McGraw-Hill, Inc., New York, Boston, 2002.
[42] Y.S. Touloukian, R.K. Kirby, E.R. Taylor, T.Y.R. Lee, Thermophysical Properties of Matter, The TPRC Data Series, Purdue University, 1977.
[43] R. Morrell, Handbook of Properties of Technical and Engineering Ceramics, Stationery Office Books, London, 1987.
[44] G.J. Janz, Molten Salts Handbook, Elsevier, New York, 1967.
[45] Dynalene Molten Salts, Dynalene, Inc., 2016, https://www.dynalene.com/Molten-Salts-s/1831.htm.
[46] J. Gao, Y. Wang, Y. Ping, D. Hu, G. Xu, F. Gu, F. Su, A thermodynamic analysis of methanation reactions of carbon oxides for the production of synthetic natural gas, RSC Adv. 2 (2012) 2358.
[47] Wabash Power Equipment Company. 510 KW Dresser-Rand Turbodyne, (2017) https://www.wabashpower.com/inventory/turbine-generators/steam-turbines/510-kw-dresser-rand-turbodyne.
[48] Rheinhutte Pumps. Pumps for Molten Salts, (2017) http://www.rh-pumps.com/pump-application/molten-salts/.
[49] J. Turner, G. Sverdrup, M.K. Mann, P.-C. Maness, B. Kroposki, M. Ghirardi, R.J. Evans, D. Blake, Renewable hydrogen production, Int. J. Energy Res. 32 (2008) 379–407.
[50] U.S. Department of Energy, Energy Department Announces $14 Million to Advance Hydrogen Fuel Technologies, (2016) https://energy.gov/eere/articles/energy-department-announces-14-million-advance-hydrogen-fuel-technologies.
[51] M. De-Saint-Jean, P. Baurens, C. Bouallou, K. Couturier, Economic assessment of a power-to-substitute natural-gas process including high-temperature steam electrolysis, Int. J. Hydrogen Energ. 40 (2015) 6487–6500.
[52] Renewable natural gas (RNG) technology roadmap for Canada, http://www.cga.ca/natural-gas-markets/renewable-natural-gas/2014.
[53] Biomethane for Transportation Opportunities for Washington State, (2013) http://www.energy.wsu.edu/Documents/Biomethane_For_Transportation_WWCleanCities.pdf.
[54] Renewable Natural Gas for Transportation: An Overview of the Feedstock Capacity, Economics, and GHG Emission Reduction Benefits of RNG as a Low-carbon Fuel, (2012) http://www.npc.org/FTF_Topic_papers/22-RNG.pdf.
[55] P. Collet, E. Flottes, A. Favre, L. Raynal, H. Pierre, S. Capela, C. Peregrina, Techno-economic and life cycle assessment of methane production via biogas upgrading and power to gas technology, Appl. Energy 192 (2017) 282–295.